Rough Wave Simulation and Validation using Onboard Ship Motion Data in the Southern Hemisphere to Enhance Ship Weather Routing

Lu, Li-Feng ; Sasa, Kenji ; Sasaki, Wataru ; Terada, Daisuke ; Kano, Toshiyuki ; Mizojiri, Takaaki

(Citation)
Ocean Engineering,144:61-77

(Issue Date)
2017-11-01

(Resource Type)
journal article

(Version)
Accepted Manuscript

(URL)
https://hdl.handle.net/20.500.14094/90005320

Rough wave simulation and validation using onboard ship motion data in the Southern Hemisphere to enhance ship weather routing

Li-Feng Lu[1], Kenji Sasa[1], Wataru Sasaki[2], Daisuke Terada[3] , Toshiyuki Kano[4] and Takaaki Mizojiri[5]

[1]Department of Maritime Science, Kobe University, 5-1-1, Fukae Minami Machi, Higashinada-ku, Kobe, Hyogo 658-0022, Japan

[2]Japan Agency for Marine-Earth Science and Technology, 3173-25, Showa Cho, Kanazawa-ku, Yokohama, Kanagawa 236-0001, Japan

[3]Department of Mechanical Systems Engineering, National Defense Academy, 1-10-20, Hashirimizu, Yokosuka, Kanagawa 239-8686, Japan

[4]National Maritime Research Institute, 6-38-1, Shinkawa, Mitaka, Tokyo 181-0004, Japan

[5]Imabari Shipbuilding Co. Ltd., 30 Showa-cho, Marugame, Kagawa 763-8511, Japan

Abstract

In this study, three cases of rough-sea navigation in the Southern Hemisphere were reproduced using the National Oceanic and Atmospheric Administration's WAVEWATCH III. Different wind inputs with various spatial and temporal resolutions were considered, originating from the National Centers for Environmental Prediction Final (NCEP-FNL) Operation Model Global Tropospheric Analyses, the European Center for Medium-range Weather Forecasts Interim Reanalysis (ERA-Interim), and the Weather Research and Forecasting (WRF) model. The simulated waves (wave hindcasts) were validated using measured onboard ship motion data. Comparisons of measured and simulated pitch motion indicated that each of the different wind inputs produced reasonable first-order estimates of rough waves. However, for application to a ship's weather routing systems, wind input selection should be carefully considered. For example, near-surface winds from the ERA-Interim underestimated rough waves, while those from the NCEP-FNL Analyses had a contrary tendency. In addition, although the wind inputs from the ERA-Interim produced wave hindcasts that is more consistent with measured results, these same inputs generally underestimated the increasing-phase pitch motion under severe weather conditions, which poses a danger for ships. Thus, the use of wind inputs from NCEP-FNL Analyses or higher-resolution WRF model is recommended for application to ship weather routing systems.

Key words: Weather routing, rough-sea navigation, wave estimation, ship motion, Southern Hemisphere

1. Introduction

Maritime transport is estimated to account for more than 90% of the world's trade by volume. As the world's trade continues to grow, maritime volumes are expected to increase (United Nations Conference on Trade and Development, 2016). Currently, the shipping industries are facing additional economic and environmental challenges. First, industrial shipping is very sensitive to bunker fuel prices. With increasing cargos and shipping routes, a high priority for ship owners is to minimize fuel oil consumption during each voyage. Second, growing concerns about global warming have increased the focus on environmental impacts from shipping. The International Maritime Organization (IMO) estimated that carbon dioxide (CO_2) emissions from international shipping accounted for approximately 3.1% of the total global emissions during 2007-2012; if no action is taken, this proportion could increase to 50–250% by 2050 (Smith et al., 2014). As a result, the Marine Environment Protection Committee (MEPC) introduced the Energy Efficiency Design Index (EEDI) as a mandatory measure to reduce shipping-related CO_2 emissions (Prpic-Orsic and Faltinsen, 2012). Enacted in 2013, the IMO is requiring all ships to reduce CO_2 emissions by 20% per tonne/km by 2020 and 50% per tonne/km by 2050 (Smith et al., 2014).

Accurate weather routing of ships has been increasingly recognized as an important contributor to safe, economical and efficient shipping. Based on forecasts of weather, sea conditions, and ship performance, weather routing determines the optimum tracks for ocean voyages, which in turn maximize safety and crew comfort, minimize fuel oil consumption and harmful emissions, and minimize travel times (Bowditch 2002). Original proposed by James (1957), ship weather routing has significantly progressed during the last few decades owing to advances in meteorological analysis, weather forecast ability, and computer modeling techniques.

Until now, studies on ship weather routing have considered ocean voyages in the North Indian Ocean (e.g., Padhy et al., 2008; Sen and Padhy, 2015), the North Atlantic Ocean (e.g., Chen, 1978;

Hinnenthal, 2008; Shao et al., 2012), the North Pacific Ocean (e.g., Hagiwara and Spaans, 1987; Takashima et al., 2009; Lin et al., 2013), and the Mediterranean Sea (e.g., Delitala et al., 2010). Few studies on ship weather routing have considered ocean voyages in the Southern Hemisphere, largely because of lower maritime transport activity and less accurate weather predictions due to sparse observation.

According to a recent report on global marine trends (QinetiQ et al., 2013), however, economic development in emerging countries and continued rapid industrialization and urbanization in developing and developed countries will increase shipping exports of manufactured products, grain, energy resources, and natural resources from countries such as Australia and Brazil to importing countries such as China and India. Consequently, container, tanker, liquefied natural gas (LNG) carrier and bulk carrier ships are expected to navigate the Southern Hemisphere more often in the next 15 years. Therefore, the provision of effective and efficient ship weather routing in the Southern Hemisphere has become urgent and important.

The increasing availability of remotely sensed data has enabled significant advances in the accuracy and reliability of weather and wave simulation in the Southern Hemisphere. For example, Gorman et al. (2003) applied wind output from the European Center for Medium-range Weather Forecasts (ECMWF) to the WAve Model (WAM) and simulated the generation and propagation of deep-water waves in New Zealand from 1979 to 1998 with a spatial resolution of 1.125°. More recently, Bosserelle et al. (2012) applied the National Oceanic and Atmospheric Administration's (NOAA) WAVE WATCH III (WW3) model using reanalysis wind field data from the National Centers for Environmental Prediction/National Center for Atmospheric Research (NCEP/NCAR) to quantify the long-term wave variability in coastal seas around Western Australia with a grid size of 1/6°. Similarly, Durrant et al. (2014) applied the WW3 model using wind data from the NCEP Climate Forecast System Reanalysis (CFSR) to conduct a 31-year (1979–2009) wave hindcast in

coastal seas around Australia and islands of the South Pacific Ocean with a minimum grid size of 1/15°. Their model was later applied to the south coastal area of Australia and presented good agreement with a moored buoy observation (Rapizo et al., 2015).

Each of these studies has provided fundamental wave information in the Southern Hemisphere. However, given the high frequency of storm occurrences in the Southern Hemisphere, the spatial and temporal resolutions of these prior wave simulations may be too coarse for application to ship weather routing systems, especially under rough weather conditions. Moreover, the validation of wave fields relies on either remote satellite data that has limited space and time coverage or moored buoy data that is confined to coastal areas. Until recently, access to onboard data that describes real-time wave effects on ship performance during rough-sea navigation in the Southern Hemisphere, has been limited. As noted by Vettor and Guedes Soares (2016), the number of observations remains insufficient to draw reliable conclusions for ship routing systems from wind and wave analyses in the Southern Hemisphere.

Beginning in 2010, we have conducted long-term observations on weather, wave, ship motion, navigation and engine performance using a 20,000 DWT class bulk carrier during many rough weather events in both the Southern and the Northern Hemispheres. Using these data, Sasa et al. (2015) presented two case studies of rough-sea navigation in the Northern Hemisphere that showed good agreement between simulated and observed waves. Building upon this earlier work, we used the corresponding ship motion measurement in this study to evaluate the accuracy of the wave hindcasts under much more severe weather in the Southern Hemisphere when radar failed to measure waves correctly. Prior studies have demonstrated wave estimation from measured ship motion using wave buoy analogy (Neilsen, 2008). However, no such studies have considered real sea navigation. In this study, we selected three cases of rough-sea navigation in 2013, and simulated the waves using NOAA's WW3 model and three different wind inputs with various spatial and

temporal resolutions. A comparison of the simulated and observed results enabled (1) validation of the simulated wind and waves using onboard measurements and observations, and (2) evaluation of the different wind input sources with respect to reliability for ship navigation and weather routing in the Southern Hemisphere, especially during rough weather.

Following this introductory information, section 2 shows the onboard observation. Section 3 describes the methods used in this study related to the wave simulation and wave validation. Section 4 presents the results of the simulated wave hindcasts and validation efforts, which compare the pitch motion of the ship as estimated from the simulated wave hindcasts with the onboard observation. Section 5 summarizes key findings from this study and suggests opportunities for future research.

2. Onboard observation

2.1 Observation system

An onboard observation has been conducted using a 28,000 DWT class bulk carrier since June 2010 to August 2016 for six years. The ship is 160.4 m long (between perpendiculars) and 27.2 m wide, with a 9.82 m fully loaded draft and a 14 knots design operational speed. Unlike higher-speed container ships, the lower-speed bulk carrier is less able to avoid rough weather and sometimes has to navigate under severe weather conditions.

Observation data from the bulk carrier includes weather data (wind speed, wind direction, etc.) measured using a weather gauge, wave data (wave height, directional wave spectrum) measured using a X-band radar, voyage parameters (ship position, speed, ship course, etc.) recorded using a voyage data recorder, engine performance data (shaft revolution, engineer power, fuel oil consumption, etc.) recorded using an engine data logger, and ship motion data (pitch, roll, and yaw) measured using an inertial measurement unit. The detail of onboard measuring is described such as

the measured parameters and observation instruments in Sasa et al. (2015). During the first two years of observation, select data, including wave observation data during March 2013 were missing due to measurement system failure. The ship's speed should be evaluated as the speed through the water. However, the measured value shows abnormal in 2012-2013 for the mechanical failure. The speed over the ground is alternatively used here.

Observation indicated that the ship encountered several rough weather events in 2013. In this study, we selected three of these events near the south coast of South Africa (Case 1), in the western South Atlantic Ocean (Case 2), and in the Tasman Sea between Australia and New Zealand (Case 3) for further investigation. Figure 1 shows the geographic location of these three rough weather events. Table 1 details these rough-sea navigation periods and the corresponding ship conditions. Figure 2 shows the 10-minute averaged measurement of wind speed (30.86 m above the water surface), ship speed, pitch motion, roll motion, engine shaft revolution, engine power, and fuel oil consumption during each of the three rough-sea navigations.

Figure 1 Rough-sea navigation cases considered in this study (black lines indicate ship routes; red circles indicate three rough weather events).

Table 1 Rough-sea navigation periods and corresponding ship conditions for Cases 1, 2, and 3 in 2013

Figure 2 Measured data for Cases 1, 2, and 3: (a) wind speed, (b) ship speed, (c) pitch motion, (d) roll motion, (e) engine shaft revolution, (f) engine power, and (g) fuel oil consumption

2.2 Case 1: south coast of South Africa (June 1–4)

In Case 1, the bulk carrier was traveling westward from the Indian Ocean to the South Atlantic Ocean along the coast of South Africa in early June 2013. Loaded condition of the ship was half loaded (mean draft is 8.16m). During this time, wind speed of approximately 20-30 m/s continued for nearly three days. Influenced by the strong winds under rough seas, the ship speed decreased from nearly 12 knots to 3 knots, resulting in the ship remaining almost stationary. At the same time, the pitch motion increased from approximately 1.5° to over 5°. Nearly 12 hours later, the roll motion increased from 4° to 14°. Despite a decrease in engine shaft revolution (110 to 95 rpm) associated with the decrease in ship speed, the engine power and fuel oil consumption maintained constant despite of very slow speed. The ship's heading has been frequently altered for 0-30° in 1-3.5 days.

2.3 Case 2: western South Atlantic Ocean (June 15)

In Case 2, the bulk carrier was traveling from South Africa to Uruguay, crossing the South Atlantic Ocean in mid-June 2013. Loaded condition was the same with Case 1 because of the same voyage. The wind speed during this period was lower than that in Case 1, peaking at 19 m/s on June 14. Approximately 12 hours later, the ship speed decreased from 12 knots to approximately 8 knots. Concurrent with the decrease in ship speed, the pitch motion increased from approximately 1.5° to 5°. Approximately 6 hours later, the roll motion also increased, peaking at 14°. As in Case 1, the engine power and fuel oil consumption maintained relatively high levels despite the decrease in main engine revolution (110 to 105 rpm) associated with the decrease in ship speed. The ship's heading has been altered with large angles from 240° to 330° in 1.8-2.2 days. This also caused rapid change of the pitch motion.

2.4 Case 3: Tasman Sea (March 15–16)

Case 3 differs substantially from Cases 1 and 2. In Case 3, the ship was traveling from the south coast of Australia to northern New Zealand, crossing the Tasman Sea in mid-March 2013. Loaded condition was relatively ballast (draft is 6.55m), because the ship was scheduled to load timbers at the next port in New Zealand. During this time, the wind speed reached just over 9 m/s, but the ship speed nonetheless experienced two successive sudden drops from 15 knots to approximately 9 knots. Concurrently, the pitch motion increased from 1° to 4.7° and the roll motion increased from approximately 4° to nearly 14°. Engine power and fuel oil consumption also markedly decreased as the engine shaft revolution decreased. The ship's heading has not been fixed in 1-2.5 days from 20° to 340°, and the error of relative wave direction might be larger if the averaged value is evaluated for 1 hour.

3.Wave simulation

3.1 Model setup

To replicate the rough waves encountered by the bulk carrier in the Southern Hemisphere in March and June 2013, we performed wave hindcasts using NOAA's third-generation WW3 model (version 4.18), which has been widely used for open ocean wave simulation. Stopa et al. (2016) tested NOAA's WW3 model using satellite measurements and buoy spectra. Their results suggested that all physical parameterizations for the wind input and whitecap dissipation in the WW3 model performed well in terms of significant wave height.

By explicitly parameterizing all physical processes, such as wind input, nonlinear wave interactions, whitecap dissipation, etc., the following spectra action balance equations can be solved (Tolman et al., 2014):

$$\frac{\partial N}{\partial t} + \nabla_x \cdot \left(\mathbf{c}_g + \mathbf{U}\right)N + \frac{\partial}{\partial k}\hat{k}N + \frac{\partial}{\partial \theta}\hat{\theta}N = \frac{S}{\sigma} \tag{1}$$

$$\hat{k} = -\frac{\partial \sigma}{\partial d}\frac{\partial d}{\partial s} - \mathbf{k} \cdot \frac{\partial \mathbf{U}}{\partial s} \tag{2}$$

$$\hat{\theta} = -\frac{1}{k}\left[\frac{\partial \sigma}{\partial d}\frac{\partial d}{\partial m} + \mathbf{k} \cdot \frac{\partial \mathbf{U}}{\partial m}\right] \tag{3}$$

where N is the vector wavenumber spectrum, $\mathbf{c}_g$ is the wave group velocity, $\mathbf{U}$ is the current velocity, s is a coordinate in the direction of θ, m is a coordinate perpendicular to s, and S is the net source term for the spectrum. In this study, S was determined as the summation of the linear input (S_{ln}), wind input (S_{in}), nonlinear wave-wave interaction (S_{nl}), wave dissipation (S_{ds}), and wave-bottom interaction (S_{bot}) terms, such that $S = S_{ln} + S_{in} + S_{nl} + S_{ds} + S_{bot}$.

Once the vector wave number spectrum is obtained, the wave direction ψ can be calculated using the following formula:

$$\psi = 2\pi - \psi_s + \tan^{-1}(b/a) \tag{4}$$

$$\begin{aligned} a &= \int_0^{2\pi}\int_0^{\infty} \cos\psi D_W(\omega,\psi) d\omega d\psi \\ b &= \int_0^{2\pi}\int_0^{\infty} \sin\psi D_W(\omega,\psi) d\omega d\psi \end{aligned} \tag{5}$$

The wave simulations were conducted using a global grid with a spatial resolution of 0.5° in longitudinal and latitudinal directions and three nested regional grids representing the South African coast, the western South Atlantic Ocean, and the Tasman Sea with a spatial resolution of 0.1°. A two-way nesting technique was applied, which takes into account the wave interactions between global and regional domains.

Figure 3 shows the bathymetry and computational domains for Case 1, 2, and3. Bathymetry data originated from the ETOPO dataset (NOAA, 2006). Sea ice coverage was considered in the global model by applying ice concentrations measured by the Nimbus-7 Scanning Multichannel Microwave Radiometer (SMMR) and the Defense Meteorological Satellite Program's (DMSP)

Special Sensor Microwave Imager (SSM/I) and Special Sensor Microwave Imager Sounder (SSMIS) (Cavalieri et al., 1996).

Figure 3 Bathymetry and computational domain for cases 1, 2, and 3.

For the net source term (S), a linear input source term (S_{ln}) was included to improve initial wave growth during initialization of the model (Cavaleri and Malanotte-Rizzoli, 1981; Tolman, 1992). The wind input (S_{in}) and wave dissipation (S_{ds}) terms were estimated using Tolman and Chalikov's (1996) method, and the nonlinear wave-wave interaction term (S_{nl}) was calculated using discrete interaction approximation (Hasselmann et al., 1985). To determine the wave-bottom interaction term (S_{bot}), an empirical linear Joint North Sea Wave Project (JONSWAP) parameterization (Hasselmann et al., 1973) was applied. Wave interactions with ocean currents and tides were not considered.

The minimum propagation time step was 330 s for the global model and 300 s for the regional models. The spectral resolution covered 36 regularly spaced directions. Frequencies extended from 0.0345 Hz with 38 frequency steps and a logarithmic frequency increment factor of 1.1. To fully initialize the WW3 model, calculations began approximately 1 month earlier than the rough-sea navigation period for each case.

Wind input is the most dominant factor in wave simulation. For ship weather routing, wind forecasts should be used to derive the predicted wave fields. In this study, our objective was, in part, to accurately replicate true rough sea states and corresponding ship motions. We considered different wind inputs with various spatial and temporal resolutions, originating from the National

Centers for Environmental Prediction Final (NCEP-FNL) Operation Model Global Tropospheric Analyses (NCEP/NWS/NOAA/U.S. Department of Commerce, 2000), the European Center for Medium-range Weather Forecasts Interim Reanalysis (ERA-Interim) (Dee et al., 2011), and the Weather Research and Forecasting (WRF) Model (Michalakes et al., 2004).

The NCEP-FNL analyses offers 1° × 1° grids covering the global region while ERA-Interim offers a spatial resolution of approximately 80 km (0.7°). Both of these wind input sources are updated every 6 hr. In addition, both of these wind input sources have assimilated multiple buoy measurements and remote satellite data. Sasaki (2016) indicated that the assimilation of satellite wind data has pronounced impacts on the wind and wave fields in the Southern Ocean.

To further investigate the impact of increased spatial and temporal weather and wave data resolutions on predicted waves and ship motions, we also considered near-surface winds simulated by the WRF Model (version 3.8) for the regional wave simulations. This next-generation mesoscale numerical weather prediction system has been widely and successfully used to predict severe weather events, such as typhoons (e.g., Storm et al., 2008; Watson and Bauman III, 2008). The WRF Model's computational domain is larger than the wave model domains shown previously in Figure 3, extending approximately 3° in four directions. The NCEP-FNL Analyses data was used to determine initial and boundary conditions, and its near-surface winds were used for the global domain. The spatial resolution and output time interval were set to be 0.1° and 3 hr, respectively. The WRF Model single moment 3-class scheme (Hong et al., 2004) was applied to determine atmospheric microphysical processes. Longwave and shortwave radiations were estimated using the rapid radiative transfer model (Mlawer et al., 1997) and Dudhia scheme (Dudhia, 1989), respectively. To determine the planetary boundary layer and cumulus parameterization, the Kain-Fritsch (Kain, 2004) and Yonsei University (Hong et al., 2006) schemes were adopted, respectively. It is necessary to compare these winds with measured one at the same altitude. The measured wind

speed is transformed to that at 10 m using Smith's method (Smith, 1988). The corrected values at 10 m altitude are used from this chapter.

Considering that wave model results are very sensitive to wind inputs, a number of prior studies have considered the validity of simulated waves based on NCEP-FNL Analyses or ERA-Interim wind input sources. For example, Tolman et al. (2002) indicated that application of NOAA's WW3 model using wind inputs from the NCEP's operational global data assimilation system and operational medium-range forecast system provided a good estimation of significant wave height. Feng et al. (2006) indicated that simulated waves based on wind inputs from the NCEP/NCAR reanalysis were more consistent with the satellite observation. More recently, Stopa and Cheung (2014) compared simulated wind and wave fields based on wind inputs from the ERA-Interim and the NCEP Climate Forecast System Reanalysis (CFSR). They found that the use of the ERA-Interim wind input data generally resulted in underestimated wind speeds and wave heights. The use of the NCEP-CFSR wind input resulted in better estimates of extreme events despite its positive bias. Campos and Guedes Soares (2016) also observed that, despite producing reasonable estimates during moderate conditions, the use of the ERA-Interim wind input resulted in some underestimation during extreme events, which may pose a risk to ships if applied in navigation applications. These studies considered conditions in the Northern Hemisphere or in the low latitudes of the Southern Hemisphere. Few studies have attempted to simulate and validate waves and their effect on ship weather routing for oceans in the mid- or high- latitude Southern Hemisphere.

In this study, we utilized the ship's onboard observations while operating in the Southern Hemisphere to evaluate the accuracy of simulated waves using different wind inputs and discussed their applicability for ship weather routing under severe weather conditions.

3.2 Wave validation

We have found that radar measured wave heights and spectrum lack reliability when wave heights exceed 4 m (details are shown in section 4). Moreover, wave observation data during March 2013 were missing due to measurement system failure. Therefore, we validated the simulated waves by comparing the ship motions estimated from the simulated wave hindcasts with those measured onboard. Prior studies have shown that ship motion measurements can be used to estimate sea states even when high-frequency wave components of wind wave spectrum are considered (Nielsen, 2008).

In this study, we focused on the ship's pitch motion because of its vital role in ship safety and its close relationship to ship speed [as shown previously in Figure 2 (b–c)]. Assuming that the ship motion was proportional to the directional wave spectrum, we have

$$D_P(\omega,\theta,V)=\frac{\left|X_P(\omega,\theta,V)\right|^2}{\left|1-2\omega_0 V\cos\theta/g\right|}D_W(\omega_0,\theta) \tag{6}$$

where $D_P(\omega,\theta,V)$ is the directional pitch spectrum (ω is the encounter circular frequency, θ is the relative wave direction, and V is the ship speed), $D_W(\omega_0,\theta)$ is the directional wave spectrum (ω_0 is the circular frequency of incident waves), and $X_P(\omega,\theta,V)$ is the response function of pitch motion. Several seakeeping models exist to calculate the response function of pitch motion. In this study, we used the Enhanced Unified Theory (EUT) (Kashiwagi, 1997) and the New Strip Method (NSM) (Salvessen et al., 1970), both of which are considered more practical in terms of computational cost and accuracy. Figure 4 shows the frequency response functions of pitch at 0°, 30°, 60°, and 90° by the EUT and the NSM.

Figure 4 Computed results of frequency response functions of pitch motion (Case 1 and 2, 0-90°)

It is obvious that amplitudes are nearly zero at high frequency region (ω>1.2 rad/s), and the pitch motion does not respond in short wave periods. The values are larger for 0.2-0.4 in the NSM than those in the EUT.

Based on the assumption that the ship's motion follows a Rayleigh distribution, the significant amplitude of pitch (pitch motion) ($PA_{1/3}$) and the corresponding average period (PT_{02}) can be calculated as follows:

$$PA_{1/3} = 4.00\sqrt{\int_0^{2\pi}\int_0^{\infty} D_P(\omega,\theta,V)d\omega d\theta} \tag{7}$$

$$PT_{02} = 2\pi \frac{\sqrt{\int_0^{2\pi}\int_0^{\infty} D_P(\omega,\theta,V)d\omega d\theta}}{\sqrt{\int_0^{2\pi}\int_0^{\infty} \omega^2 D_P(\omega,\theta,V)d\omega d\theta}} \tag{8}$$

4. Wave hindcast results and wave validation

As an initial task in this study, wave hindcasts were performed for each of the three rough weather events considered. The results of these hindcasts related to significant wave height, wave period as well as wind speed and sea level pressure distribution are presented separately for each of the three cases.

4.1 Wave hindcasts results

4.1.1 Case 1: south coast of South Africa (June 1-4)

Figure 5 compares the simulated wind directions and speeds at 10 m above the water surface and parallel to the ship's track based on the NCEP-FNL Analyses, ERA-Interim, and WRF Model wind inputs with the onboard observation. These results indicated that each of the simulation models generally underestimated the wind speed relative to the onboard observation. Consistent with onboard observation, the WRF Model estimated a maximum wind speed of approximately 23 m/s at 2 days. However, the NCEP-FNL Analyses and ERA-Interim consistently underestimated

the wind speed by approximately 3-9 m/s and 4-8 m/s, respectively, during the rough weather event (June 1–4). NCEP-FNL Analyses and WRF presented about 70° deviation in the wind direction during June 1-4, while about 35° for ERA-Interim.

Figure 5 Comparison of observed and simulated wind directions and speeds for Case 1.

Figure 6 compares the simulated wave directions, significant wave heights and wave periods based on the three different wind inputs with the onboard observation for June 1-4, 2013. Prior to the rough weather event (0-1 day), significant wave heights of < 4 m and wave periods of approximately 6 s were consistently estimated by each of the models and measured onboard. During the rough weather event (2-3 days), the measured wave height remained at <4 m, despite observed wind speeds of > 20 m/s. This unreasonably low measured wave height may be attributable to poor performance of the radar analyzer during severe weather; when the pitch motion is too high, the microwave radiation cannot accurately detect the sea surface ahead. During this same time, each of the simulation models estimated more reasonable wave heights of 5-7 m. Specifically, a peak wave height of nearly 8 m was estimated at 2.3 days using the WRF Model wind input, while a peak wave height of approximately 5.5 m was estimated nearly 8 hours later using the ERA-Interim wind input. Coinciding with the ERA-Interim peak wave time, a peak of nearly 7 m was estimated using the NCEP-FNL Analyses wind input.

Figure 6 Comparison of observed and simulated wave directions, significant wave heights and wave periods for Case 1.

Regarding the wave period, each of the simulation models consistently estimated longer wave periods relative to observation. Maximum simulated wave periods during the rough weather event

(2-3 days) were approximately 10 s, 9 s, and 10 s based on the NCEP-FNL Analyses, ERA-Interim, and WRF Model wind inputs, respectively. Comparatively, the measured wave period remained constant throughout the observation period at approximately 6 s; this measurement may not be reliable because of the poor radar performance during severe weather.

All the simulated wave direction showed the similar results and comparable with the observation during the rough sea navigation (1-2 days). The differences decreased from about 70° at 06:00 June 2 to about 10 ° at 22:00 June 3.

Measured at three distinct times during the rough weather event (00:00 June 2, 00:00 June 3, and 00:00 June 4), Figure 7 shows the sea level pressure distribution using data from the NCEP-FNL Analyses and the simulated wave heights and wave directions and wind vectors based on the three different wind inputs. In this case, as the ship navigated westward and approached South Africa's east coast, low pressure developed to the south of South Africa and propagated eastward [Figure 7(a)]. Concurrently, high waves exceeding 10 m propagated eastward along South Africa's south coast. In this situation, the ship is said to be navigating in a *head sea* condition, and violent pitch motion is expected.

Figure 7 Snapshot sea level pressure distributions and comparative simulated wave fields for Case 1 (shaded areas denote significant wave height, red arrows denote wave direction, black arrows denote wind vector, and black dot denote the ship position).

Comparing the waves generated by the three different wind inputs, strong waves up to 10 m to the west of South Africa were estimated based on the NCEP-FNL Analyses wind input. The estimated height of these waves decreased over time as they propagated toward the coast of South Africa [Figure 7(b1)]. Conversely, the simulated waves based on WRF Model wind input generally

gained strength as they are approached the coast [Figure 7(b2)]. The simulated waves based on the ERA-Interim were generally smaller relative to the other two simulation results [Figure 7(b3)].

4.1.2 Case 2: western South Atlantic Ocean (June 15)

Figure 8 compares the simulated wind directions and speeds based on the NCEP-FNL Analyses, ERA-Interim, and WRF Model wind inputs with the onboard observation. The simulation models reasonably replicated the temporal variation of the observed wind speed but underestimated the true wind speed by 4-10 m/s. The peak wind speed estimated using the WRF Model wind input occurred at approximately at the same time as the observed peak wind speed, while the peak wind speeds estimated using the NCEP-FNL Analyses and ERA-Interim wind inputs occurred approximately 9 hours later. This difference in results suggested that the higher spatial and temporal resolutions offered by the WRF Model more accurately estimated small-scale spatial variation in wind speed. The simulated wind directions showed the similar results and their deviation from the observation decreased from about 45° to 0° during the rough sea navigation (1-2 days).

Figure 8 Comparison of observed and simulated wind directions and speeds for Case 2.

Figure 9 compares the simulated significant wave heights, wave period and wave directions based on the three different wind inputs with the onboard observation. The observed wave height and period was <4 m and approximately 6 s, respectively. Each of the simulation models reasonably replicated the temporal variation of the wave heights, although estimated significant wave heights following the rough weather event (1-2 days) were higher than those measured onboard. Comparatively, the estimated wave periods were considerably overestimated relative to the wave periods measured onboard. The simulate wave directions were comparable with the observation

during the first one and half days, but failed to reproduce the sudden change in wave direction at 11:00 and 20:00 on June 15 as indicated by the observation.

Figure 9 Comparison of observed and simulated wave directions, significant wave heights and wave periods for Case 2.

Again measured at three distinct times during the rough weather event (00:00 June 15, 12:00 June 15, and 00:00 June 16), Figure 10 shows the sea level pressure distribution using data from the NCEP-FNL Analyses and the simulated wave heights and directions and wind vectors based on the three different wind inputs. Weather conditions in this case were similar to the weather conditions in Case 1 [Figure 10(a)]. As low pressure developed between South America and Antarctica and propagated northeastward, the ocean waves in western South Atlantic Ocean propagated northeastward. The ship, navigating westward, encountered strong waves from forward left.

Figure 10 Snapshot sea level pressure distributions and comparative simulated wave fields for Case 2 (shaded areas denote significant wave height, red arrows denote wave direction, black arrows denote wind vector, and black dot denote the ship position).

Comparing the waves generated by the three different wind inputs, the largest and smallest waves were estimated based on the NCEP-FNL Analyses [Figure 10(b1)] and ERA-Interim [Figure 10(b2)] wind inputs, respectively. Simulated waves using the WRF Model wind input were intermediate [Figure 10(b3)] relative to the other two simulation results.

4.1.3 Case 3: Tasman Sea (March 14-17)

As noted previously, select data, including wave observation data in March 2013, were missing because of measurement system failure limiting wave-related comparisons between simulated and observed results. Nonetheless, Case 3 demonstrates some unique phenomena worthy of consideration. For example, despite relatively moderate winds, the ship experienced violent motions. Figure 11 shows the ship's track in mid-March, 2013. The ship departs from a Southern Australian port, and is heading for Northern New Zealand though Tasman Sea. During the voyage, the ship has altered its course irregularly and the track seems a very complicated zigzag path. Simultaneously pitch and roll motions have increased with the speed loss, and the ship's captain confirmed that they were in a dangerous situation. To determine the cause of the violent ship motion, we considered the simulated sea states.

Figure 11 Ship track in mid-March 2013 from Australia to New Zealand through Tasman Sea.

Figure 12 compares the simulated wind speeds based on the NCEP-FNL Analyses, ERA-Interim, and WRF Model wind inputs with the onboard observation. The measured wind speed was relatively low (<10 m/s). Comparatively, the estimated wind speeds were consistently higher for each of the simulation models. Peak wind speeds of approximately 11 m/s occurring at approximately noon on March 15 were estimated using the NCEP-FNL Analyses and ERA-Interim wind inputs. Both models showed minimal variation during the observation period. Conversely, a peak wind speed of >13 m/s occurring at 18:00 on March 15 was estimated using the WRF Model wind input. The WRF Model simulation results also exhibited much more variation over time. All the simulated wind directions presented much more smooth results and could not reproduce the

abrupt variation in wind direction during rough sea navigation (1-2 days) as observation indicated. This could be attributed to the rough time resolution in each model.

Figure 12 Comparison of observed and simulated wind speeds and directions for Case 3.

Figure 13 compares the simulated wave directions, significant wave heights and wave periods based on the three different wind inputs; no onboard observation data was available. Each of the simulation models exhibited an abrupt increase in wave height beginning at 00:00 on March 15. Similar singular estimated wave height peaks (>4 m/s occurring at 9:00 on March 15) were estimated based on the NCEP-FNL Analyses and ERA-Interim wind inputs. Comparatively, dual estimated wave height peaks were estimated based on the WRF Model wind input; the wave height increased twice successively to reach a peak value of approximately 5.5 m at 01:00 on March 16.

Figure 13 Comparison of simulated wave directions, significant wave heights and wave periods for Case 3.

Simulated wave period results were more consistent among the three simulation models. Estimated wave periods increased from 6 to >10 s during the first day. Wave period estimates based on the WRF Model wind input exhibited a similar but less pronounced dual-peaking tendency with a small subsequent peak reaching nearly 10 s at the end of day on March 15.

All the simulated wave directions were consistent and presented 4-times sudden change in wave direction on March 15. WRF Model showed as large as about 30° deviation from the other two results on March 14 and about 90° deviation on March 16.

Measured at three distinct times during the rough weather event (12:00 March 15, 00:00 March 16, and 12:00 March 16), Figure 14 shows the sea level pressure distribution using data from the NCEP-FNL Analyses and the simulated wave heights and directions and wind vectors based on the three different wind inputs. In this case, two areas of low pressure were located north and southwest of the Tasman Sea. Wave heights were relatively high in these two areas, and the waves propagated southward and northeastward.

Figure 14 Snapshot sea level pressure distributions and comparative simulated wave fields for Case 3 (shaded areas denote significant wave height, red arrows denote wave direction, black arrows denote wind vector, and black dot denote the ship position).

The ship, navigating northeastward from the south coast of Australia to northern New Zealand, first encountered the northern area of low pressure, which moved southward and generated relatively large waves of approximately 6m [Figure 13(b1–b3) at 12:00 on March 15]. Approximately 12 hours later, a strong swell propagating from the southwest to the northeast with a maximum wave height of >7 m entered the Tasman Sea and interacted with existing southward waves [Figure 13 (b1–b3) at 00:00 on March 16]. During this time, the ship was in between the two waves and was pushed northward under their interaction. After another 12 hours, the northeastward swell emerged as the dominant wave and the ship navigated farther northeastward [Figure 13(b1–b3) at 12:00 on March 16].

Despite the lack of wave observation data for comparison, the simulated wave hindcasts indicated that the ship encountered two opposite-direction waves during the rough weather event. This encounter may explain the observed decreases in ship speed and increases in pitch and roll motions shown previously in Figure 2. Comparing the simulated wave fields generated by the three

different wind inputs, the estimated wave heights for waves propagating from north to south were higher based on the WRF Model wind input relative to the other two simulation model results.

4.2 Wave validation

The observed wave heights measured by radar in Case 1 and 2 were suspect, indicating unreasonably low values during rough-sea navigation. As such, these measurements were not deemed appropriate for validation of simulated waves. Moreover, observed wave heights were not available in Case 3 because of measurement system failure. Instead, wave validation was performed by comparing the pitch motion of the ship as estimated from the simulated wave hindcasts with the pitch motion measured onboard.

4.2.1 Case 1: south coast of South Africa (June 1–4)

Figure 15 compares the calculated pitch motion using EUT and NSM methods and based on radar measurements and wave hindcasts using the NCEP-FNL Analyses, ERA-Interim, and WRF Model wind inputs with onboard observations for Case 1. Because the radar failed to measure waves >4 m, the corresponding calculated pitch motion was also unreasonable small (<3°) when compared with the observed pitch motion. The calculated pitch motions based on the simulated wave hindcasts were more reasonable. However, the calculated pitch motions based on the NCEP-FNL Analyses and WRF Model wind inputs during June 3–4 (1.5–2.5 days) generally overestimated the true pitch by 2° and 1°, respectively. Although the calculated pitch motion based on the ERA-Interim wind input was most consistent with the observed pitch motion, this model underestimated pitch motion by approximately 1° during the increasing phase of the rough weather event (from the end of June 2 to the beginning of June 3), which could pose a danger to ships if

applied for weather routing. Comparing EUT and NSM methods, the calculated pitch motion was comparable but relatively higher using the former method.

Figure 15 Comparison of observed and calculated pitch motions based on radar measurements and simulated wave hindcasts using EUT (top) and NSM (bottom) methods for Case 1.

Figure 16 compares the RMS of significant pitch amplitude using EUT and NSM methods, respectively for Case 1. Results indicated that the ERA-Interim wind input gives the smallest error, while NCEP-FNL Analyses and WRF Model wind inputs result in relative larger error. When applying radar measurement, the error was largest since it failed to measure big waves.

Figure 16 Comparison of RMS of significant pitch amplitude using EUT and NSM methods for Case 1.

To further investigate the ship's pitch motion, Figure 17 compares the calculated pitch frequency spectrums using EUT and NSM methods and based on radar measurements and wave hindcasts using the three different wind inputs with onboard observations at 6:00 on June 3. Although the calculated pitch frequency spectrums based on the simulated wave hindcasts were more concentrated in the lower frequency bands, the observed spectral peak was well replicated at approximately 0.7 rad/s. The calculated pitch frequency spectrums using the EUT and NSM methods were similar, although the calculated spectral peak was higher using EUT method.

Figure 17 Comparison of observed and calculated pitch frequency spectrums based on radar measurements and simulated wave hindcasts using EUT (left) and NSM (right) methods for case 1 at 6:00 on June 3 2013.

4.2.2 Case 2: western South Atlantic Ocean (June 15)

Figure 18 compares the calculated pitch motion using EUT and NSM methods and based on radar measurements and wave hindcasts using the three different wind input sources with onboard observations for Case 2. Similar to Case 1, the radar measurements underestimated the pitch motion, particularly when the NSM method was applied. The calculated pitch motions based on the NCEP-FNL Analyses wind input during June 15 generally overestimated the true pitch by 1-2°, respectively. The calculated pitch motion based on the WRF model wind input was most consistent with the observed pitch motion. The rapid change of pitch motion can be simulated in each method by using the 10-minute averaged value on ship's heading. Generally, the calculated pitch motions using EUT method is relatively higher than that using NSM method. Comparatively, use of the NSM method better captured the pitch motion during the rough weather event's increasing phase irrespective of wind inputs.

Figure 18 Comparison of observed and calculated pitch motions based on radar measurements and simulated wave hindcasts using EUT (top) and NSM (bottom) methods for Case 2.

Figure 19 compares the RMS of significant pitch amplitude using EUT and NSM methods, respectively for Case 2. Results based on the ERA-Interim and WRF model wind inputs give relatively small error, while NCEP-FNL wind inputs result in larger error. Similar to Case 1, when applying radar measurement, the error was largest since it failed to measure big waves.

Figure 19 Comparison of RMS of significant pitch amplitude using EUT and NSM methods for Case 2.

Figure 20 compares the calculated pitch frequency spectrums using EUT and NSM methods and based on radar measurements and wave hindcasts using the three different wind inputs with onboard observations at 12:00 on June 15. The calculated pitch frequency spectrums based on the simulated wave hindcasts were more consistent with observed pitch frequency spectrum at frequencies <0.5 rad/s than the calculated pitch frequency spectrum based on the radar measurement, which was much lower. EUT and NSM methods resulted in similar spectrum shapes. Similar to Case 1, the pitch frequency spectral peak calculated using EUT method was relative higher than the peak calculated using the NSM method, resulting in the relative higher pitch motion as shown previously in Figure 18.

Figure 20 Comparison of observed and calculated pitch frequency spectrums based on radar measurements and simulated wave hindcasts using EUT (left) and NSM (right) methods for Case 2 at 12:00 on June 15 2013.

4.2.3 Case 3: Tasman Sea (March 15–16)

Figure 21 compares the calculated pitch motion using EUT and NSM methods and based on wave hindcasts using the three different wind inputs with onboard observations for Case 3. The observation indicated that the pitch motion increased twice during March 15, and the calculated pitch motions reasonably replicated the two increasing of true pitch motion. However, all the calculated pitch motion during the beginning of March 15 underestimated the true pitch from 0.5° to 1°. During the end of March 15 (the second increasing of pitch motion), the calculated pitch

motions based on the NCEP-FNL Analyses was comparable with the observation. However, the calculated pitch motion based on the ERA-Interim was underestimated by approximately 1°. Conversely, the calculated pitch motion based on WRF model wind input was overestimated by approximately 2°. It is the reason why the simulated wave height is higher for 2 m in the WRF wind input than that in other methods, as shown in Figure 13. It implicates that the wind distribution computed on WRF model overestimates true winds than those on the linear interpolated wind inputs for this case. Similar to Case 1 and 2, the calculated pitch motion using EUT method was relatively higher than that using NSM method.

Figure 21 Comparison of observed and calculated pitch motions based on simulated wave hindcasts using EUT (top) and NSM (bottom) methods for Case 3.

Figure 22 compares the RMS of significant pitch amplitude using EUT and NSM methods, respectively for Case 3. Results based on the NCEP-FNL and ERA-Interim wind input give relatively small error, while WRF model wind inputs result in larger error since it overestimated pitch amplitude during the second increasing phase of pitch motion.

Figure 22 Comparison of RMS of significant pitch amplitude using EUT and NSM methods for Case 3.

To further investigate these differences, Figure 23 compares the calculated pitch frequency spectrums using EUT and NSM methods and based on wave hindcasts using the three different wind inputs with onboard observations at 3:00 on March 15. Similar to Case 1 and 2, the calculated pitch frequency spectrums based on the simulated wave hindcasts were more concentrated in the lower frequency bands. Use of the both EUT and NSM method resulted in overestimation of the

true pitch frequency spectrums between frequencies of 0.45-0.65 rad/s, and underestimation of the true pitch frequency spectrums at frequencies > 0.65 rad/s. Using either method, the calculated pitch frequency spectrum was general relatively low based on the WRF Model wind input, consistent with its lower pitch motion peak shown previously in Fig. 20. Similar to Case 1 and 2, the pitch frequency spectrum calculated using EUT method was relative higher than the peak calculated using the NSM method.

Figure 23 Comparison of observed and calculated pitch frequency spectrums based on simulated wave hindcasts using EUT (left) and NSM (right) methods for Case 3 at 3:00 on March 15 2013.

5. Conclusions

In this study, we simulated wave hindcasts using NCEP-FNL Analyses, ERA-Interim, and WRF Model wind inputs with various spatial and temporal resolutions for three cases of rough-sea navigation in the Southern Hemisphere. The simulated waves were validated using onboard ship motion measurements. Comparisons of the observed and calculated pitch motions indicated that the simulated wave hindcasts reasonably replicated rough waves, suggesting potential application to ship weather routing under severe weather conditions.

Wind speed comparisons indicated that, for relatively high wind speeds, each of the simulation models based on the three different wind input sources tended to underestimate the true wind speeds by up to approximately 10 m/s. Wind speed estimates based on the ERA-Interim wind input were consistently lower than the estimates based on the NCEP-FNL Analyses wind input. The increased spatial and temporal resolutions offered by the WRF Model wind input tended to improve the accuracy of wind speed estimates and provided greater detail regarding wind speed variation.

Corresponding to the wind speed, the simulated waves using the NCEP-FNL Analyses wind input were generally higher than the waves estimated using the ERA-Interim wind input, and consequently generated more violent ship motion. This result is consistent with other study findings (e.g. Campos and Guedes Soares, 2016). Results also indicated that the simulated waves using the higher-resolution WRF Model wind input both overestimated and underestimated the wave height and ship motion, depending on the case. Increased spatial resolution of WW3 model can improve estimation accuracy.

The calculation of pitch motions in rough weather events is sensitivity to relative wave direction. Supplemental investigations confirmed that average of ship direction measurement every 1 hour is not appropriate for the calculation of pitch motions using wave hindcasts when ship course changes frequently under the rough sea condition. Average of ship direction by shorter time interval such as 10 min is better in such cases.

In conclusion, by using onboard ship motion measurements, we have effectively validated efforts to simulate rough waves in the Southern Hemisphere. The results suggest that near-surface winds from the ERA-Interim generally underestimated rough waves, while those from the NCEP-FNL Analyses had a contrary tendency. In addition, although the wind inputs from the ERA-Interim produced simulated wave hindcasts more consistent with measured results, these same inputs generally underestimated the increasing-phase pitch motion under severe weather conditions, which poses a danger for ships. Thus, the use of wind inputs from the NCEP-FNL Analyses or higher-resolution WRF Model is recommended for application to ship weather routing systems under severe weather conditions in the Southern Hemisphere.

Acknowledgement

We appreciate the assistance of Shoei Kisen Kaisha Ltd., Northstar Shipping Management Ltd., the bulk carrier's crew, and shipping agents in Singapore and Australia in conducting this study. In

addition, we would like to thank Mr. Keiichi Hirayama, Japan Radio Ltd., for his advice on radar wave measurement. This study was sponsored by the Japan Society for the Promotion of Science (JSPS) through its Grants-in-Aid for Scientific Research (Scientific Research B) program titled "A new optimum shipping system integrated with safety, economy, and ocean environment for international maritime shipping" (No. 25282103) and the Fundamental Research Developing Association for Shipbuilding and Offshore (REDAS) titled "Accurate estimation of wave spectrum and ship performance in rough seas in the Southern Hemisphere using two step validations of sea clutter of Radar" (REDAS16-4(7)).

References

Alves, J.-H.G.M., "Numerical modeling of ocean swell contributions to the global wind-wave climate", *J. Ocean Modelling* 11, pp.98–122, 2006.

Bosserelle, C., Pattiaratchi, C., and Haigh, I., "Inter-annual variability and longer-term changes in the wave climate of Western Australia between 1970 and 2009", *J. Ocean Dynamics, Vol.62*, pp.63–76, 2012.

Bowditch, N., "The American Practical Navigator: an epitome of navigation"*, National Imagery and Mapping Agency*, *Paradise Cay Publications,* p.896, 2002.

Campos, R.M. and Guedes Soares, C., "Comparison of HIPOCAS and ERA wind and wave reanalyses in the North Atlantic Ocean", *J. Ocean Engineering* Vol.112, pp.320–334, 2016.

Cavaleri, L. and Malanotte-Rizzoli, P., "Wind-wave prediction in shallow water: theory and applications," *Journal of Geophysical Research*, *Vol.86*, pp.10961–10973, 1981.

Cavalieri, D.J., Parkinson, C.L., Gloersen, P., and Zwally, H.J. (Updated annually). "Sea Ice Concentrations from Nimbus-7 SMMR and DMSP SSM/I-SSMIS Passive Microwave Data, Version 1. Boulder, Colorado, United States", *NASA National Snow and Ice Center Distributed Active Archive Center*, Doi: http://dx.doi.org/10.5067/8GQ8LZQVLOVL, 1996.

Chen, H., "A dynamic program for minimum cost ship routing under uncertainty", *Ph.D. Thesis*, *Department of Ocean Engineering, Massachusetts Institute of Technology*, *Cambridge*, *Massachusetts*, 1978.

Delitala, A.M.S., Gallino, S., Villa, L., Lagouvardos, K., and Drago, A., "Weather routing in long-distance Mediterranean routes", *Theoretical and Applied Climatology*, *Vol.102*, pp.125–137, 2010.

Dee, D. P., Uppala, S. M., Simmons, A. J., Berrisford, P., Poli, P., Kobayashi, S., Andrae, U., Balmaseda, M. A., Balsamo, G., Bauer, P., Bechtold, P., Beljaars, A. C. M., van de Berg, L., Bidlot, J., Bormann, N., Delsol, C., Dragani, R., Fuentes, M., Geer, A. J., Haimberger, L., Healy, S. B., Hersbach, H., Hólm, E. V., Isaksen, L., Kållberg, P., Köhler, M., Matricardi, M., McNally, A. P., Monge-Sanz, B. M., Morcrette, J.-J., Park, B.-K., Peubey, C., de Rosnay, P., Tavolato, C., Thépaut, J.-N., and Vitart, F., "The ERA-Interim reanalysis: configuration and performance of the data assimilation system", *Quarterly Journal of the Royal Meteorological Society*, Vol.137, pp.553–597, doi: 10.1002/qj.828, 2011

Dudhia, J., "Numerical study of convection observed during the winter monsoon experiment using a mesoscale two-dimensional model", *Journal of the Atmospheric Sciences*, *Vol.46*, *No.20*, pp. 3077–3107, 1989.

Durrant T., Greenslade, D., Hemer, M., and Trenham, C., "A global wave hindcast focused on the central and south Pacific", *Collaboration for Australian Weather and Climate Research (CAWCR) Technical Report*, *No. 070*, p. 45, 2014.

Feng, H., Vandermark, D., Quilfen, Y., Chapron, B., and Beckley, B., "Assessment of wind-forcing impact on a global wind-wave model using the TOPEX altimeter", *J. Ocean Engineering Vol.33*, *No.11-12,* pp.1431–1461, 2006.

Gorman, R.M., Bryan, K.R., and Laing, A.K., "Wave hindcast for the New Zealand region: Deep-water wave climate", *New Zealand Journal of Marine and Freshwater Research*, *Vol.37*, pp.589–612, 2003.

Hagiwara, H. and Spaans, J.A., "Practical weather routing of sail-assisted motor vessels", *Journal of Navigation*, *Vol.40*, *No.1*, pp.96–119, 1987.

Hasselmann, K., Barnett, T.P., Bouws, E., Carlson, H., Cartwright, D.E., Enke, K., Ewing, J.A., Gienapp, H., Hasselmann, D.E., Kruseman, P., Meerburg, A., Müller, P., Olbers, D.J., Richter, K., Sell, W., and Walden, H., "Measurements of wind-wave growth and swell decay during the Joint North Sea Wave Project (JONSWAP)", *Ergänzungsheft zur Deutschen Hydrographischen Zeitschrift, Reihe,* A(8)12, p. 95, 1973.

Hasselmann, S., Hasselmann, K., Allender, J.H., and Barnett, T.P., "Computations and parameterizations of the nonlinear energy transfer in a gravity-wave spectrum, Part II: parameterizations of the nonlinear energy transfer for application in wave models", *Journal of Physical Oceanography*, *Vol.15*, pp.1378–1391, 1985.

Hinnenthal, J., "Robust Pareto – Optimum Routing of Ships utilizing Deterministic and Ensemble Weather Forecasts", *Ph.D. Thesis, Berlin University of Technology*, p. 133, 2008.

Hong, S.-Y., Dudhia, J., and Chen, S.-H, "A revised approach to ice microphysical processes for the bulk parameterization of clouds and precipitation", *Monthly Weather Review*, *Vol.132*, *No.1*, pp. 103–132, 2004.

Hong, S.-Y., Noh, Y., and Dudhia, J., "A new vertical diffusion package with an explicit treatment of entrainment processes", *Monthly Weather Review*, *Vol.134*, *No.9*, pp.2318–2341, 2006.

James, R.W., "Application of Wave Forecasts to Marine Navigation", *U.S. Naval Oceanographic Office*, *Naval Science and Technological Laboratory (NSTL)*, 1957.

Kain, J.S., "The Kain-Fritsch convective parameterization: an update", *Journal of Applied Metrotology*, *Vol.43*, *No.1*, pp.170–181, 2004.

Kashiwagi, M., "Numerical seakeeping calculations based on the slender ship theory", *J. Ship Technology Research*, *Vol.44*, *No.4*, pp.167–192, 1997.

Lin, Y.-H., Fang, M.-C., and Yeung, R.W., "The optimization of ship weather-routing algorithm based on the composite influence of multi-dynamic elements", *J. Applied Ocean Research*, *Vol.43*, pp.184–194, 2013.

Michalakes, J., Dudhia, J., Gill, D., Henderson, T., Klemp, J., Skamarock, W., and Wang, W., "The weather research and forecast model: software architecture and performance", *Proceedings of the 11th ECMWF Workshop on the Use of High Perfomance Computing in Meteorology*, pp.25–29 October 2004, Reading, U.K., Ed. George Mozdzynski, 2004.

Mlawer, E.J., Taubman, S.J., Brown, P.D., Iacono, M.J., and Clough, S.A., "Radiative transfer for inhomogeneous atmospheres: RRTM, a validated correlated-k model for the longwave", *Journal of Geophysical Research Vol.102*, *D14*, pp.16663–16682, 1997.

Nielsen, U.D., "The wave buoy analogy–estimating high-frequency wave excitations", *J. Applied Ocean Research*, *Vol.30*, pp.100–106, 2008.

National Oceanic and Atmospheric Administration (NOAA), "National Geophysical Data Center, Etopo2v2 global gridded 2-minute database", 2006.

National Centers for Environmental Prediction/National Weather Service/NOAA/U.S. Department of Commerce, "NCEP FNL Operational Model Global Tropospheric Analyses, continuing from July 1999", *Research Data Archive at the National Center for Atmospheric Research*, *Computational and Information Systems Laboratory*. https://doi.org/10.5065/D6M043C6, 2000 (updated daily)

Padhy, C.P., Sen, D., and Bhaskaran, P.K., "Application of wave model for weather routing of ships in the North Indian Ocean", *Natural Hazards*, *Vol.44*, pp.373–385, 2008.

Prpić-Oršić, J. and Faltinsen, O.M., "Estimation of ship speed loss and associated CO_2 emissions in a seaway", *J. Ocean Engineering*, *Vol.44*, pp.1–10, 2012.

Qinetiq, Lloyd's Register Group Limited, and the University of Strathclyde, "Global Marine Trends 2030", 2013.

Rapizo, H., Babanin, A.V., Schulz, E., Hemer, M.A., and Durrant, T.H., "Observation of wind-waves from a moored buoy in the Southern Ocean", *J. Ocean Dynamics*, *Vol.65*, pp.1275–1288, 2015.

Salvesen, N., Tuck, E.O., and Faltinsen, O., "Ship motions and sea loads", *Proceedings of the Society of Naval Architects and Marine Engineers*, Vol,78, pp.250–287, 1970.

Sasa, K., Terada, D., Shiotani, S., Wakabayashi, N., Ikebuchi, T., Chen, C., Takayama, A., and Uchida, M., "Evaluation of ship performance in international maritime transportation using an onboard measurement system–in case of a bulk carrier in international voyages", *J. Ocean Engineering*, *Vol.104*, pp.294–309, 2015.

Sasaki, W., "Impact of satellite data assimilation in atmospheric reanalysis on the marine wind and wave climate", *Journal of Climate*, *Vol.29*, pp.6351–6361, 2016.

Sen, D. and Padhy, C.P., "An approach for development of a ship routing algorithm for application in the North Indian Ocean region", *J. Applied Ocean Research*, *Vol.50*, pp.173–191, 2015.

Smith, S.D., "Coefficients for sea surface wind stress, heat flux and wind profiles as a function of speed and temperature", *Journal of Geographic Research*, *Vol.93*, *No. C12*, pp.467-472, 1988.

Smith, T.W.P., Jalkanen, J.P., Anderson, B.A., Corbett, J.J., Faber, J., Hanayama, S., O'Keeffe, E., Parker, S., Johansson, L., Aldous, L., Raucci, C., Traut, M., Ettinger, S., Nelissen, D., Lee, D.S., Ng, S., Agrawal, A., Winebrake, J.J., Hoen, M., Chesworth, S., and Pandey, A., "Third IMO Greenhouse Gas Study 2014"*, International Maritime Organization (IMO)*, June 2014, p. 328, 2014.

Storm, B., Dudhia, J., Basu, S., Swift, A., and Giammanco, I., "Evaluation of the weather research and forecasting model on forecasting low-level jets: implications for wind energy". *Wind Energy*, *Vol.12*, *No.1*, pp.81–90. DOI: 10.1002/we.288, 2008.

Stopa, J.E., Ardhuin, F., Babanin, A., and Zieger, S., "Comparison and validation of physical wave parameterizations in spectral wave models", *J. Ocean Modelling*, *Vol.103*, pp.2–17, 2016.

Stopa, J.E. and Cheung, K.F., "Intercomparison of wind and wave data from the ECMWF Reanalysis Interim and the NCEP Climate Forecast System Reanalysis", *J. Ocean Modelling*, *Vol.75*, pp.65–83, 2014.

Shao, W., Zhou, P., and Thong, S.K., "Development of a novel forward dynamic programming method for weather routing", *Journal of Marine Science and Technology*, *Vol.17*, *No.2*, pp.239–251, 2012.

Takashima, K., Mezaoui, B., and Shoji, R., "On the fuel saving operation for coastal merchant ships using weather routing", *International Journal on Marine Navigation and Safety of Sea Transportation*, *Vol.3*, *No.4*, pp.401–406, 2009.

Tolman, H.L., "Effects of numerics on the physics in a third-generation wind-wave model", *Journal of Physical Oceanography*, *Vol.22*, pp.1095–1111, 1992.

Tolman, H.L., Balasubramaniyan, B., Burroughs, L.D., Chalikov, D.V., Chao, Y.Y., Chen, H.S., and Gerald, V.M., "Development and implementation of wind-generated ocean surface wave models at NCEP", *Weather and Forecasting*, *Vol.17*, pp.311–333, 2002.

Tolman, H.L., "User manual and system documentation of WAVEWATCH III, version 4.18", *National Oceanic and Atmospheric Administration/National Weather Service/National Centers for Environmental Prediction (NOAA/NWS/NCEP) Technical Note*, p.282, 2014.

Tolman, H.L. and Chalikov, D., "Source terms in a third-generation wind wave model", *Journal of Physical Oceanography*, *Vol.26*, pp.2497–2518, 1996.

United Nations Conference on Trade and Development (UNCTAD), "Review of Maritime Transport 2016", *UNCTAD/Review of Maritime Transport (RMT) 2016*, *United Nations Conference on Trade and Development*, *Geneva*, *Switzerland*, p. 104, 2016.

Vettor, R. and Guedes Soares, C., "Rough weather avoidance effect on the wave climate experienced by oceangoing vessels", *J. Applied Ocean Research*, *Vol.59*, pp.606–615, 2016.

Watson, L.R. and Bauman III, W.H., "Weather Research and Forecasting Model Wind Sensitivity Study at Edwards Air Force Base, CA", *National Aeronautics and Space Administration Contractor Report, NASA/CR-2008-214755*, 2008.

Rough wave simulation and validation using onboard ship motion data in the Southern Hemisphere to enhance ship weather routing

Li-Feng Lu[1], Kenji Sasa[1], Wataru Sasaki[2], Daisuke Terada[3] , Toshiyuki Kano[4] and Takaaki Mizojiri[5]

[1]Department of Maritime Science, Kobe University, 5-1-1, Fukae Minami Machi, Higashinada-ku, Kobe, Hyogo 658-0022, Japan

[2]Japan Agency for Marine-Earth Science and Technology, 3173-25, Showa Cho, Kanazawa-ku, Yokohama, Kanagawa 236-0001, Japan

[3]Department of Mechanical Systems Engineering, National Defense Academy, 1-10-20, Hashirimizu, Yokosuka, Kanagawa 239-8686, Japan

[4]National Maritime Research Institute, 6-38-1, Shinkawa, Mitaka, Tokyo 181-0004, Japan

[5]Imabari Shipbuilding Co. Ltd., 30 Showa-cho, Marugame, Kagawa 763-8511, Japan

Abstract

In this study, three cases of rough-sea navigation in the Southern Hemisphere were reproduced using the National Oceanic and Atmospheric Administration's WAVEWATCH III. Different wind inputs with various spatial and temporal resolutions were considered, originating from the National Centers for Environmental Prediction Final (NCEP-FNL) Operation Model Global Tropospheric Analyses, the European Center for Medium-range Weather Forecasts Interim Reanalysis (ERA-Interim), and the Weather Research and Forecasting (WRF) model. The simulated waves (wave hindcasts) were validated using measured onboard ship motion data. Comparisons of measured and simulated pitch motion indicated that each of the different wind inputs produced reasonable first-order estimates of rough waves. However, for application to a ship's weather routing systems, wind input selection should be carefully considered. For example, near-surface winds from the ERA-Interim underestimated rough waves, while those from the NCEP-FNL Analyses had a contrary tendency. In addition, although the wind inputs from the ERA-Interim produced wave hindcasts that is more consistent with measured results, these same inputs generally underestimated the increasing-phase pitch motion under severe weather conditions, which poses a danger for ships. Thus, the use of wind inputs from NCEP-FNL Analyses or higher-resolution WRF model is recommended for application to ship weather routing systems.

Key words: Weather routing, rough-sea navigation, wave estimation, ship motion, Southern Hemisphere

1. Introduction

Maritime transport is estimated to account for more than 90% of the world's trade by volume. As the world's trade continues to grow, maritime volumes are expected to increase (United Nations Conference on Trade and Development, 2016). Currently, the shipping industries are facing additional economic and environmental challenges. First, industrial shipping is very sensitive to bunker fuel prices. With increasing cargos and shipping routes, a high priority for ship owners is to minimize fuel oil consumption during each voyage. Second, growing concerns about global warming have increased the focus on environmental impacts from shipping. The International Maritime Organization (IMO) estimated that carbon dioxide (CO_2) emissions from international shipping accounted for approximately 3.1% of the total global emissions during 2007-2012; if no action is taken, this proportion could increase to 50–250% by 2050 (Smith et al., 2014). As a result, the Marine Environment Protection Committee (MEPC) introduced the Energy Efficiency Design Index (EEDI) as a mandatory measure to reduce shipping-related CO_2 emissions (Prpic-Orsic and Faltinsen, 2012). Enacted in 2013, the IMO is requiring all ships to reduce CO_2 emissions by 20% per tonne/km by 2020 and 50% per tonne/km by 2050 (Smith et al., 2014).

Accurate weather routing of ships has been increasingly recognized as an important contributor to safe, economical and efficient shipping. Based on forecasts of weather, sea conditions, and ship performance, weather routing determines the optimum tracks for ocean voyages, which in turn maximize safety and crew comfort, minimize fuel oil consumption and harmful emissions, and minimize travel times (Bowditch 2002). Original proposed by James (1957), ship weather routing has significantly progressed during the last few decades owing to advances in meteorological analysis, weather forecast ability, and computer modeling techniques.

Until now, studies on ship weather routing have considered ocean voyages in the North Indian Ocean (e.g., Padhy et al., 2008; Sen and Padhy, 2015), the North Atlantic Ocean (e.g., Chen, 1978;

Hinnenthal, 2008; Shao et al., 2012), the North Pacific Ocean (e.g., Hagiwara and Spaans, 1987; Takashima et al., 2009; Lin et al., 2013), and the Mediterranean Sea (e.g., Delitala et al., 2010). Few studies on ship weather routing have considered ocean voyages in the Southern Hemisphere, largely because of lower maritime transport activity and less accurate weather predictions due to sparse observation.

According to a recent report on global marine trends (QinetiQ et al., 2013), however, economic development in emerging countries and continued rapid industrialization and urbanization in developing and developed countries will increase shipping exports of manufactured products, grain, energy resources, and natural resources from countries such as Australia and Brazil to importing countries such as China and India. Consequently, container, tanker, liquefied natural gas (LNG) carrier and bulk carrier ships are expected to navigate the Southern Hemisphere more often in the next 15 years. Therefore, the provision of effective and efficient ship weather routing in the Southern Hemisphere has become urgent and important.

The increasing availability of remotely sensed data has enabled significant advances in the accuracy and reliability of weather and wave simulation in the Southern Hemisphere. For example, Gorman et al. (2003) applied wind output from the European Center for Medium-range Weather Forecasts (ECMWF) to the WAve Model (WAM) and simulated the generation and propagation of deep-water waves in New Zealand from 1979 to 1998 with a spatial resolution of 1.125°. More recently, Bosserelle et al. (2012) applied the National Oceanic and Atmospheric Administration's (NOAA) WAVE WATCH III (WW3) model using reanalysis wind field data from the National Centers for Environmental Prediction/National Center for Atmospheric Research (NCEP/NCAR) to quantify the long-term wave variability in coastal seas around Western Australia with a grid size of 1/6°. Similarly, Durrant et al. (2014) applied the WW3 model using wind data from the NCEP Climate Forecast System Reanalysis (CFSR) to conduct a 31-year (1979–2009) wave hindcast in

coastal seas around Australia and islands of the South Pacific Ocean with a minimum grid size of 1/15°. Their model was later applied to the south coastal area of Australia and presented good agreement with a moored buoy observation (Rapizo et al., 2015).

Each of these studies has provided fundamental wave information in the Southern Hemisphere. However, given the high frequency of storm occurrences in the Southern Hemisphere, the spatial and temporal resolutions of these prior wave simulations may be too coarse for application to ship weather routing systems, especially under rough weather conditions. Moreover, the validation of wave fields relies on either remote satellite data that has limited space and time coverage or moored buoy data that is confined to coastal areas. Until recently, access to onboard data that describes real-time wave effects on ship performance during rough-sea navigation in the Southern Hemisphere, has been limited. As noted by Vettor and Guedes Soares (2016), the number of observations remains insufficient to draw reliable conclusions for ship routing systems from wind and wave analyses in the Southern Hemisphere.

Beginning in 2010, we have conducted long-term observations on weather, wave, ship motion, navigation and engine performance using a 20,000 DWT class bulk carrier during many rough weather events in both the Southern and the Northern Hemispheres. Using these data, Sasa et al. (2015) presented two case studies of rough-sea navigation in the Northern Hemisphere that showed good agreement between simulated and observed waves. Building upon this earlier work, we used the corresponding ship motion measurement in this study to evaluate the accuracy of the wave hindcasts under much more severe weather in the Southern Hemisphere when radar failed to measure waves correctly. Prior studies have demonstrated wave estimation from measured ship motion using wave buoy analogy (Neilsen, 2008). However, no such studies have considered real sea navigation. In this study, we selected three cases of rough-sea navigation in 2013, and simulated the waves using NOAA's WW3 model and three different wind inputs with various spatial and

temporal resolutions. A comparison of the simulated and observed results enabled (1) validation of the simulated wind and waves using onboard measurements and observations, and (2) evaluation of the different wind input sources with respect to reliability for ship navigation and weather routing in the Southern Hemisphere, especially during rough weather.

Following this introductory information, section 2 shows the onboard observation. Section 3 describes the methods used in this study related to the wave simulation and wave validation. Section 4 presents the results of the simulated wave hindcasts and validation efforts, which compare the pitch motion of the ship as estimated from the simulated wave hindcasts with the onboard observation. Section 5 summarizes key findings from this study and suggests opportunities for future research.

2. Onboard observation

2.1 Observation system

An onboard observation has been conducted using a 28,000 DWT class bulk carrier since June 2010 to August 2016 for six years. The ship is 160.4 m long (between perpendiculars) and 27.2 m wide, with a 9.82 m fully loaded draft and a 14 knots design operational speed. Unlike higher-speed container ships, the lower-speed bulk carrier is less able to avoid rough weather and sometimes has to navigate under severe weather conditions.

Observation data from the bulk carrier includes weather data (wind speed, wind direction, etc.) measured using a weather gauge, wave data (wave height, directional wave spectrum) measured using a X-band radar, voyage parameters (ship position, speed, ship course, etc.) recorded using a voyage data recorder, engine performance data (shaft revolution, engineer power, fuel oil consumption, etc.) recorded using an engine data logger, and ship motion data (pitch, roll, and yaw) measured using an inertial measurement unit. The detail of onboard measuring is described such as

the measured parameters and observation instruments in Sasa et al. (2015). During the first two years of observation, select data, including wave observation data during March 2013 were missing due to measurement system failure. The ship's speed should be evaluated as the speed through the water. However, the measured value shows abnormal in 2012-2013 for the mechanical failure. The speed over the ground is alternatively used here.

Observation indicated that the ship encountered several rough weather events in 2013. In this study, we selected three of these events near the south coast of South Africa (Case 1), in the western South Atlantic Ocean (Case 2), and in the Tasman Sea between Australia and New Zealand (Case 3) for further investigation. Figure 1 shows the geographic location of these three rough weather events. Table 1 details these rough-sea navigation periods and the corresponding ship conditions. Figure 2 shows the 10-minute averaged measurement of wind speed (30.86 m above the water surface), ship speed, pitch motion, roll motion, engine shaft revolution, engine power, and fuel oil consumption during each of the three rough-sea navigations.

Figure 1 Rough-sea navigation cases considered in this study (black lines indicate ship routes; red circles indicate three rough weather events).

Table 1 Rough-sea navigation periods and corresponding ship conditions for Cases 1, 2, and 3 in 2013

Figure 2 Measured data for Cases 1, 2, and 3: (a) wind speed, (b) ship speed, (c) pitch motion, (d) roll motion, (e) engine shaft revolution, (f) engine power, and (g) fuel oil consumption

2.2 Case 1: south coast of South Africa (June 1–4)

In Case 1, the bulk carrier was traveling westward from the Indian Ocean to the South Atlantic Ocean along the coast of South Africa in early June 2013. Loaded condition of the ship was half loaded (mean draft is 8.16m). During this time, wind speed of approximately 20-30 m/s continued for nearly three days. Influenced by the strong winds under rough seas, the ship speed decreased from nearly 12 knots to 3 knots, resulting in the ship remaining almost stationary. At the same time, the pitch motion increased from approximately 1.5° to over 5°. Nearly 12 hours later, the roll motion increased from 4° to 14°. Despite a decrease in engine shaft revolution (110 to 95 rpm) associated with the decrease in ship speed, the engine power and fuel oil consumption maintained constant despite of very slow speed. The ship's heading has been frequently altered for 0-30° in 1-3.5 days.

2.3 Case 2: western South Atlantic Ocean (June 15)

In Case 2, the bulk carrier was traveling from South Africa to Uruguay, crossing the South Atlantic Ocean in mid-June 2013. Loaded condition was the same with Case 1 because of the same voyage. The wind speed during this period was lower than that in Case 1, peaking at 19 m/s on June 14. Approximately 12 hours later, the ship speed decreased from 12 knots to approximately 8 knots. Concurrent with the decrease in ship speed, the pitch motion increased from approximately 1.5° to 5°. Approximately 6 hours later, the roll motion also increased, peaking at 14°. As in Case 1, the engine power and fuel oil consumption maintained relatively high levels despite the decrease in main engine revolution (110 to 105 rpm) associated with the decrease in ship speed. The ship's heading has been altered with large angles from 240° to 330° in 1.8-2.2 days. This also caused rapid change of the pitch motion.

2.4 Case 3: Tasman Sea (March 15–16)

Case 3 differs substantially from Cases 1 and 2. In Case 3, the ship was traveling from the south coast of Australia to northern New Zealand, crossing the Tasman Sea in mid-March 2013. Loaded condition was relatively ballast (draft is 6.55m), because the ship was scheduled to load timbers at the next port in New Zealand. During this time, the wind speed reached just over 9 m/s, but the ship speed nonetheless experienced two successive sudden drops from 15 knots to approximately 9 knots. Concurrently, the pitch motion increased from 1° to 4.7° and the roll motion increased from approximately 4° to nearly 14°. Engine power and fuel oil consumption also markedly decreased as the engine shaft revolution decreased. The ship's heading has not been fixed in 1-2.5 days from 20° to 340°, and the error of relative wave direction might be larger if the averaged value is evaluated for 1 hour.

3.Wave simulation

3.1 Model setup

To replicate the rough waves encountered by the bulk carrier in the Southern Hemisphere in March and June 2013, we performed wave hindcasts using NOAA's third-generation WW3 model (version 4.18), which has been widely used for open ocean wave simulation. Stopa et al. (2016) tested NOAA's WW3 model using satellite measurements and buoy spectra. Their results suggested that all physical parameterizations for the wind input and whitecap dissipation in the WW3 model performed well in terms of significant wave height.

By explicitly parameterizing all physical processes, such as wind input, nonlinear wave interactions, whitecap dissipation, etc., the following spectra action balance equations can be solved (Tolman et al., 2014):

$$\frac{\partial N}{\partial t} + \nabla_x \cdot \left(\mathbf{c}_g + \mathbf{U}\right)N + \frac{\partial}{\partial k}\hat{k}N + \frac{\partial}{\partial \theta}\hat{\theta}N = \frac{S}{\sigma} \tag{1}$$

$$\hat{k} = -\frac{\partial \sigma}{\partial d}\frac{\partial d}{\partial s} - \mathbf{k} \cdot \frac{\partial \mathbf{U}}{\partial s} \tag{2}$$

$$\hat{\theta} = -\frac{1}{k}\left[\frac{\partial \sigma}{\partial d}\frac{\partial d}{\partial m} + \mathbf{k} \cdot \frac{\partial \mathbf{U}}{\partial m}\right] \tag{3}$$

where N is the vector wavenumber spectrum, $\mathbf{c}_g$ is the wave group velocity, $\mathbf{U}$ is the current velocity, s is a coordinate in the direction of θ, m is a coordinate perpendicular to s, and S is the net source term for the spectrum. In this study, S was determined as the summation of the linear input (S_{ln}), wind input (S_{in}), nonlinear wave-wave interaction (S_{nl}), wave dissipation (S_{ds}), and wave-bottom interaction (S_{bot}) terms, such that $S = S_{ln} + S_{in} + S_{nl} + S_{ds} + S_{bot}$.

Once the vector wave number spectrum is obtained, the wave direction ψ can be calculated using the following formula:

$$\psi = 2\pi - \psi_s + \tan^{-1}(b/a) \tag{4}$$

$$\begin{aligned} a &= \int_0^{2\pi}\int_0^{\infty} \cos\psi D_W(\omega,\psi) d\omega d\psi \\ b &= \int_0^{2\pi}\int_0^{\infty} \sin\psi D_W(\omega,\psi) d\omega d\psi \end{aligned} \tag{5}$$

The wave simulations were conducted using a global grid with a spatial resolution of 0.5° in longitudinal and latitudinal directions and three nested regional grids representing the South African coast, the western South Atlantic Ocean, and the Tasman Sea with a spatial resolution of 0.1°. A two-way nesting technique was applied, which takes into account the wave interactions between global and regional domains.

Figure 3 shows the bathymetry and computational domains for Case 1, 2, and3. Bathymetry data originated from the ETOPO dataset (NOAA, 2006). Sea ice coverage was considered in the global model by applying ice concentrations measured by the Nimbus-7 Scanning Multichannel Microwave Radiometer (SMMR) and the Defense Meteorological Satellite Program's (DMSP)

Special Sensor Microwave Imager (SSM/I) and Special Sensor Microwave Imager Sounder (SSMIS) (Cavalieri et al., 1996).

Figure 3 Bathymetry and computational domain for cases 1, 2, and 3.

For the net source term (S), a linear input source term (S_{ln}) was included to improve initial wave growth during initialization of the model (Cavaleri and Malanotte-Rizzoli, 1981; Tolman, 1992). The wind input (S_{in}) and wave dissipation (S_{ds}) terms were estimated using Tolman and Chalikov's (1996) method, and the nonlinear wave-wave interaction term (S_{nl}) was calculated using discrete interaction approximation (Hasselmann et al., 1985). To determine the wave-bottom interaction term (S_{bot}), an empirical linear Joint North Sea Wave Project (JONSWAP) parameterization (Hasselmann et al., 1973) was applied. Wave interactions with ocean currents and tides were not considered.

The minimum propagation time step was 330 s for the global model and 300 s for the regional models. The spectral resolution covered 36 regularly spaced directions. Frequencies extended from 0.0345 Hz with 38 frequency steps and a logarithmic frequency increment factor of 1.1. To fully initialize the WW3 model, calculations began approximately 1 month earlier than the rough-sea navigation period for each case.

Wind input is the most dominant factor in wave simulation. For ship weather routing, wind forecasts should be used to derive the predicted wave fields. In this study, our objective was, in part, to accurately replicate true rough sea states and corresponding ship motions. We considered different wind inputs with various spatial and temporal resolutions, originating from the National

Centers for Environmental Prediction Final (NCEP-FNL) Operation Model Global Tropospheric Analyses (NCEP/NWS/NOAA/U.S. Department of Commerce, 2000), the European Center for Medium-range Weather Forecasts Interim Reanalysis (ERA-Interim) (Dee et al., 2011), and the Weather Research and Forecasting (WRF) Model (Michalakes et al., 2004).

The NCEP-FNL analyses offers 1° × 1° grids covering the global region while ERA-Interim offers a spatial resolution of approximately 80 km (0.7°). Both of these wind input sources are updated every 6 hr. In addition, both of these wind input sources have assimilated multiple buoy measurements and remote satellite data. Sasaki (2016) indicated that the assimilation of satellite wind data has pronounced impacts on the wind and wave fields in the Southern Ocean.

To further investigate the impact of increased spatial and temporal weather and wave data resolutions on predicted waves and ship motions, we also considered near-surface winds simulated by the WRF Model (version 3.8) for the regional wave simulations. This next-generation mesoscale numerical weather prediction system has been widely and successfully used to predict severe weather events, such as typhoons (e.g., Storm et al., 2008; Watson and Bauman III, 2008). The WRF Model's computational domain is larger than the wave model domains shown previously in Figure 3, extending approximately 3° in four directions. The NCEP-FNL Analyses data was used to determine initial and boundary conditions, and its near-surface winds were used for the global domain. The spatial resolution and output time interval were set to be 0.1° and 3 hr, respectively. The WRF Model single moment 3-class scheme (Hong et al., 2004) was applied to determine atmospheric microphysical processes. Longwave and shortwave radiations were estimated using the rapid radiative transfer model (Mlawer et al., 1997) and Dudhia scheme (Dudhia, 1989), respectively. To determine the planetary boundary layer and cumulus parameterization, the Kain-Fritsch (Kain, 2004) and Yonsei University (Hong et al., 2006) schemes were adopted, respectively. It is necessary to compare these winds with measured one at the same altitude. The measured wind

speed is transformed to that at 10 m using Smith's method (Smith, 1988). The corrected values at 10 m altitude are used from this chapter.

Considering that wave model results are very sensitive to wind inputs, a number of prior studies have considered the validity of simulated waves based on NCEP-FNL Analyses or ERA-Interim wind input sources. For example, Tolman et al. (2002) indicated that application of NOAA's WW3 model using wind inputs from the NCEP's operational global data assimilation system and operational medium-range forecast system provided a good estimation of significant wave height. Feng et al. (2006) indicated that simulated waves based on wind inputs from the NCEP/NCAR reanalysis were more consistent with the satellite observation. More recently, Stopa and Cheung (2014) compared simulated wind and wave fields based on wind inputs from the ERA-Interim and the NCEP Climate Forecast System Reanalysis (CFSR). They found that the use of the ERA-Interim wind input data generally resulted in underestimated wind speeds and wave heights. The use of the NCEP-CFSR wind input resulted in better estimates of extreme events despite its positive bias. Campos and Guedes Soares (2016) also observed that, despite producing reasonable estimates during moderate conditions, the use of the ERA-Interim wind input resulted in some underestimation during extreme events, which may pose a risk to ships if applied in navigation applications. These studies considered conditions in the Northern Hemisphere or in the low latitudes of the Southern Hemisphere. Few studies have attempted to simulate and validate waves and their effect on ship weather routing for oceans in the mid- or high- latitude Southern Hemisphere.

In this study, we utilized the ship's onboard observations while operating in the Southern Hemisphere to evaluate the accuracy of simulated waves using different wind inputs and discussed their applicability for ship weather routing under severe weather conditions.

3.2 Wave validation

We have found that radar measured wave heights and spectrum lack reliability when wave heights exceed 4 m (details are shown in section 4). Moreover, wave observation data during March 2013 were missing due to measurement system failure. Therefore, we validated the simulated waves by comparing the ship motions estimated from the simulated wave hindcasts with those measured onboard. Prior studies have shown that ship motion measurements can be used to estimate sea states even when high-frequency wave components of wind wave spectrum are considered (Nielsen, 2008).

In this study, we focused on the ship's pitch motion because of its vital role in ship safety and its close relationship to ship speed [as shown previously in Figure 2 (b–c)]. Assuming that the ship motion was proportional to the directional wave spectrum, we have

$$D_P(\omega,\theta,V)=\frac{|X_P(\omega,\theta,V)|^2}{|1-2\omega_0 V\cos\theta/g|}D_W(\omega_0,\theta) \tag{6}$$

where $D_P(\omega,\theta,V)$ is the directional pitch spectrum (ω is the encounter circular frequency, θ is the relative wave direction, and V is the ship speed), $D_W(\omega_0,\theta)$ is the directional wave spectrum (ω_0 is the circular frequency of incident waves), and $X_P(\omega,\theta,V)$ is the response function of pitch motion. Several seakeeping models exist to calculate the response function of pitch motion. In this study, we used the Enhanced Unified Theory (EUT) (Kashiwagi, 1997) and the New Strip Method (NSM) (Salvessen et al., 1970), both of which are considered more practical in terms of computational cost and accuracy. Figure 4 shows the frequency response functions of pitch at 0°, 30°, 60°, and 90° by the EUT and the NSM.

Figure 4 Computed results of frequency response functions of pitch motion (Case 1 and 2, 0-90°)

It is obvious that amplitudes are nearly zero at high frequency region (ω>1.2 rad/s), and the pitch motion does not respond in short wave periods. The values are larger for 0.2-0.4 in the NSM than those in the EUT.

Based on the assumption that the ship's motion follows a Rayleigh distribution, the significant amplitude of pitch (pitch motion) ($PA_{1/3}$) and the corresponding average period (PT_{02}) can be calculated as follows:

$$PA_{1/3} = 4.00\sqrt{\int_0^{2\pi}\int_0^{\infty} D_P(\omega,\theta,V)d\omega d\theta} \tag{7}$$

$$PT_{02} = 2\pi\frac{\sqrt{\int_0^{2\pi}\int_0^{\infty} D_P(\omega,\theta,V)d\omega d\theta}}{\sqrt{\int_0^{2\pi}\int_0^{\infty} \omega^2 D_P(\omega,\theta,V)d\omega d\theta}} \tag{8}$$

4. Wave hindcast results and wave validation

As an initial task in this study, wave hindcasts were performed for each of the three rough weather events considered. The results of these hindcasts related to significant wave height, wave period as well as wind speed and sea level pressure distribution are presented separately for each of the three cases.

4.1 Wave hindcasts results

4.1.1 Case 1: south coast of South Africa (June 1-4)

Figure 5 compares the simulated wind directions and speeds at 10 m above the water surface and parallel to the ship's track based on the NCEP-FNL Analyses, ERA-Interim, and WRF Model wind inputs with the onboard observation. These results indicated that each of the simulation models generally underestimated the wind speed relative to the onboard observation. Consistent with onboard observation, the WRF Model estimated a maximum wind speed of approximately 23 m/s at 2 days. However, the NCEP-FNL Analyses and ERA-Interim consistently underestimated

the wind speed by approximately 3-9 m/s and 4-8 m/s, respectively, during the rough weather event (June 1–4). NCEP-FNL Analyses and WRF presented about 70° deviation in the wind direction during June 1-4, while about 35° for ERA-Interim.

Figure 5 Comparison of observed and simulated wind directions and speeds for Case 1.

Figure 6 compares the simulated wave directions, significant wave heights and wave periods based on the three different wind inputs with the onboard observation for June 1-4, 2013. Prior to the rough weather event (0-1 day), significant wave heights of < 4 m and wave periods of approximately 6 s were consistently estimated by each of the models and measured onboard. During the rough weather event (2-3 days), the measured wave height remained at <4 m, despite observed wind speeds of > 20 m/s. This unreasonably low measured wave height may be attributable to poor performance of the radar analyzer during severe weather; when the pitch motion is too high, the microwave radiation cannot accurately detect the sea surface ahead. During this same time, each of the simulation models estimated more reasonable wave heights of 5-7 m. Specifically, a peak wave height of nearly 8 m was estimated at 2.3 days using the WRF Model wind input, while a peak wave height of approximately 5.5 m was estimated nearly 8 hours later using the ERA-Interim wind input. Coinciding with the ERA-Interim peak wave time, a peak of nearly 7 m was estimated using the NCEP-FNL Analyses wind input.

Figure 6 Comparison of observed and simulated wave directions, significant wave heights and wave periods for Case 1.

Regarding the wave period, each of the simulation models consistently estimated longer wave periods relative to observation. Maximum simulated wave periods during the rough weather event

(2-3 days) were approximately 10 s, 9 s, and 10 s based on the NCEP-FNL Analyses, ERA-Interim, and WRF Model wind inputs, respectively. Comparatively, the measured wave period remained constant throughout the observation period at approximately 6 s; this measurement may not be reliable because of the poor radar performance during severe weather.

All the simulated wave direction showed the similar results and comparable with the observation during the rough sea navigation (1-2 days). The differences decreased from about 70° at 06:00 June 2 to about 10 ° at 22:00 June 3.

Measured at three distinct times during the rough weather event (00:00 June 2, 00:00 June 3, and 00:00 June 4), Figure 7 shows the sea level pressure distribution using data from the NCEP-FNL Analyses and the simulated wave heights and wave directions and wind vectors based on the three different wind inputs. In this case, as the ship navigated westward and approached South Africa's east coast, low pressure developed to the south of South Africa and propagated eastward [Figure 7(a)]. Concurrently, high waves exceeding 10 m propagated eastward along South Africa's south coast. In this situation, the ship is said to be navigating in a *head sea* condition, and violent pitch motion is expected.

Figure 7 Snapshot sea level pressure distributions and comparative simulated wave fields for Case 1 (shaded areas denote significant wave height, red arrows denote wave direction, black arrows denote wind vector, and black dot denote the ship position).

Comparing the waves generated by the three different wind inputs, strong waves up to 10 m to the west of South Africa were estimated based on the NCEP-FNL Analyses wind input. The estimated height of these waves decreased over time as they propagated toward the coast of South Africa [Figure 7(b1)]. Conversely, the simulated waves based on WRF Model wind input generally

gained strength as they are approached the coast [Figure 7(b2)]. The simulated waves based on the ERA-Interim were generally smaller relative to the other two simulation results [Figure 7(b3)].

4.1.2 Case 2: western South Atlantic Ocean (June 15)

Figure 8 compares the simulated wind directions and speeds based on the NCEP-FNL Analyses, ERA-Interim, and WRF Model wind inputs with the onboard observation. The simulation models reasonably replicated the temporal variation of the observed wind speed but underestimated the true wind speed by 4-10 m/s. The peak wind speed estimated using the WRF Model wind input occurred at approximately at the same time as the observed peak wind speed, while the peak wind speeds estimated using the NCEP-FNL Analyses and ERA-Interim wind inputs occurred approximately 9 hours later. This difference in results suggested that the higher spatial and temporal resolutions offered by the WRF Model more accurately estimated small-scale spatial variation in wind speed. The simulated wind directions showed the similar results and their deviation from the observation decreased from about 45° to 0° during the rough sea navigation (1-2 days).

Figure 8 Comparison of observed and simulated wind directions and speeds for Case 2.

Figure 9 compares the simulated significant wave heights, wave period and wave directions based on the three different wind inputs with the onboard observation. The observed wave height and period was <4 m and approximately 6 s, respectively. Each of the simulation models reasonably replicated the temporal variation of the wave heights, although estimated significant wave heights following the rough weather event (1-2 days) were higher than those measured onboard. Comparatively, the estimated wave periods were considerably overestimated relative to the wave periods measured onboard. The simulate wave directions were comparable with the observation

during the first one and half days, but failed to reproduce the sudden change in wave direction at 11:00 and 20:00 on June 15 as indicated by the observation.

Figure 9 Comparison of observed and simulated wave directions, significant wave heights and wave periods for Case 2.

Again measured at three distinct times during the rough weather event (00:00 June 15, 12:00 June 15, and 00:00 June 16), Figure 10 shows the sea level pressure distribution using data from the NCEP-FNL Analyses and the simulated wave heights and directions and wind vectors based on the three different wind inputs. Weather conditions in this case were similar to the weather conditions in Case 1 [Figure 10(a)]. As low pressure developed between South America and Antarctica and propagated northeastward, the ocean waves in western South Atlantic Ocean propagated northeastward. The ship, navigating westward, encountered strong waves from forward left.

Figure 10 Snapshot sea level pressure distributions and comparative simulated wave fields for Case 2 (shaded areas denote significant wave height, red arrows denote wave direction, black arrows denote wind vector, and black dot denote the ship position).

Comparing the waves generated by the three different wind inputs, the largest and smallest waves were estimated based on the NCEP-FNL Analyses [Figure 10(b1)] and ERA-Interim [Figure 10(b2)] wind inputs, respectively. Simulated waves using the WRF Model wind input were intermediate [Figure 10(b3)] relative to the other two simulation results.

4.1.3 Case 3: Tasman Sea (March 14-17)

As noted previously, select data, including wave observation data in March 2013, were missing because of measurement system failure limiting wave-related comparisons between simulated and observed results. Nonetheless, Case 3 demonstrates some unique phenomena worthy of consideration. For example, despite relatively moderate winds, the ship experienced violent motions. Figure 11 shows the ship's track in mid-March, 2013. The ship departs from a Southern Australian port, and is heading for Northern New Zealand though Tasman Sea. During the voyage, the ship has altered its course irregularly and the track seems a very complicated zigzag path. Simultaneously pitch and roll motions have increased with the speed loss, and the ship's captain confirmed that they were in a dangerous situation. To determine the cause of the violent ship motion, we considered the simulated sea states.

Figure 11 Ship track in mid-March 2013 from Australia to New Zealand through Tasman Sea.

Figure 12 compares the simulated wind speeds based on the NCEP-FNL Analyses, ERA-Interim, and WRF Model wind inputs with the onboard observation. The measured wind speed was relatively low (<10 m/s). Comparatively, the estimated wind speeds were consistently higher for each of the simulation models. Peak wind speeds of approximately 11 m/s occurring at approximately noon on March 15 were estimated using the NCEP-FNL Analyses and ERA-Interim wind inputs. Both models showed minimal variation during the observation period. Conversely, a peak wind speed of >13 m/s occurring at 18:00 on March 15 was estimated using the WRF Model wind input. The WRF Model simulation results also exhibited much more variation over time. All the simulated wind directions presented much more smooth results and could not reproduce the

abrupt variation in wind direction during rough sea navigation (1-2 days) as observation indicated. This could be attributed to the rough time resolution in each model.

Figure 12 Comparison of observed and simulated wind speeds and directions for Case 3.

Figure 13 compares the simulated wave directions, significant wave heights and wave periods based on the three different wind inputs; no onboard observation data was available. Each of the simulation models exhibited an abrupt increase in wave height beginning at 00:00 on March 15. Similar singular estimated wave height peaks (>4 m/s occurring at 9:00 on March 15) were estimated based on the NCEP-FNL Analyses and ERA-Interim wind inputs. Comparatively, dual estimated wave height peaks were estimated based on the WRF Model wind input; the wave height increased twice successively to reach a peak value of approximately 5.5 m at 01:00 on March 16.

Figure 13 Comparison of simulated wave directions, significant wave heights and wave periods for Case 3.

Simulated wave period results were more consistent among the three simulation models. Estimated wave periods increased from 6 to >10 s during the first day. Wave period estimates based on the WRF Model wind input exhibited a similar but less pronounced dual-peaking tendency with a small subsequent peak reaching nearly 10 s at the end of day on March 15.

All the simulated wave directions were consistent and presented 4-times sudden change in wave direction on March 15. WRF Model showed as large as about 30° deviation from the other two results on March 14 and about 90° deviation on March 16.

Measured at three distinct times during the rough weather event (12:00 March 15, 00:00 March 16, and 12:00 March 16), Figure 14 shows the sea level pressure distribution using data from the NCEP-FNL Analyses and the simulated wave heights and directions and wind vectors based on the three different wind inputs. In this case, two areas of low pressure were located north and southwest of the Tasman Sea. Wave heights were relatively high in these two areas, and the waves propagated southward and northeastward.

Figure 14 Snapshot sea level pressure distributions and comparative simulated wave fields for Case 3 (shaded areas denote significant wave height, red arrows denote wave direction, black arrows denote wind vector, and black dot denote the ship position).

The ship, navigating northeastward from the south coast of Australia to northern New Zealand, first encountered the northern area of low pressure, which moved southward and generated relatively large waves of approximately 6m [Figure 13(b1–b3) at 12:00 on March 15]. Approximately 12 hours later, a strong swell propagating from the southwest to the northeast with a maximum wave height of >7 m entered the Tasman Sea and interacted with existing southward waves [Figure 13 (b1–b3) at 00:00 on March 16]. During this time, the ship was in between the two waves and was pushed northward under their interaction. After another 12 hours, the northeastward swell emerged as the dominant wave and the ship navigated farther northeastward [Figure 13(b1–b3) at 12:00 on March 16].

Despite the lack of wave observation data for comparison, the simulated wave hindcasts indicated that the ship encountered two opposite-direction waves during the rough weather event. This encounter may explain the observed decreases in ship speed and increases in pitch and roll motions shown previously in Figure 2. Comparing the simulated wave fields generated by the three

different wind inputs, the estimated wave heights for waves propagating from north to south were higher based on the WRF Model wind input relative to the other two simulation model results.

4.2 Wave validation

The observed wave heights measured by radar in Case 1 and 2 were suspect, indicating unreasonably low values during rough-sea navigation. As such, these measurements were not deemed appropriate for validation of simulated waves. Moreover, observed wave heights were not available in Case 3 because of measurement system failure. Instead, wave validation was performed by comparing the pitch motion of the ship as estimated from the simulated wave hindcasts with the pitch motion measured onboard.

4.2.1 Case 1: south coast of South Africa (June 1–4)

Figure 15 compares the calculated pitch motion using EUT and NSM methods and based on radar measurements and wave hindcasts using the NCEP-FNL Analyses, ERA-Interim, and WRF Model wind inputs with onboard observations for Case 1. Because the radar failed to measure waves >4 m, the corresponding calculated pitch motion was also unreasonable small (<3°) when compared with the observed pitch motion. The calculated pitch motions based on the simulated wave hindcasts were more reasonable. However, the calculated pitch motions based on the NCEP-FNL Analyses and WRF Model wind inputs during June 3–4 (1.5–2.5 days) generally overestimated the true pitch by 2° and 1°, respectively. Although the calculated pitch motion based on the ERA-Interim wind input was most consistent with the observed pitch motion, this model underestimated pitch motion by approximately 1° during the increasing phase of the rough weather event (from the end of June 2 to the beginning of June 3), which could pose a danger to ships if

applied for weather routing. Comparing EUT and NSM methods, the calculated pitch motion was comparable but relatively higher using the former method.

Figure 15 Comparison of observed and calculated pitch motions based on radar measurements and simulated wave hindcasts using EUT (top) and NSM (bottom) methods for Case 1.

Figure 16 compares the RMS of significant pitch amplitude using EUT and NSM methods, respectively for Case 1. Results indicated that the ERA-Interim wind input gives the smallest error, while NCEP-FNL Analyses and WRF Model wind inputs result in relative larger error. When applying radar measurement, the error was largest since it failed to measure big waves.

Figure 16 Comparison of RMS of significant pitch amplitude using EUT and NSM methods for Case 1.

To further investigate the ship's pitch motion, Figure 17 compares the calculated pitch frequency spectrums using EUT and NSM methods and based on radar measurements and wave hindcasts using the three different wind inputs with onboard observations at 6:00 on June 3. Although the calculated pitch frequency spectrums based on the simulated wave hindcasts were more concentrated in the lower frequency bands, the observed spectral peak was well replicated at approximately 0.7 rad/s. The calculated pitch frequency spectrums using the EUT and NSM methods were similar, although the calculated spectral peak was higher using EUT method.

Figure 17 Comparison of observed and calculated pitch frequency spectrums based on radar measurements and simulated wave hindcasts using EUT (left) and NSM (right) methods for case 1 at 6:00 on June 3 2013.

4.2.2 Case 2: western South Atlantic Ocean (June 15)

Figure 18 compares the calculated pitch motion using EUT and NSM methods and based on radar measurements and wave hindcasts using the three different wind input sources with onboard observations for Case 2. Similar to Case 1, the radar measurements underestimated the pitch motion, particularly when the NSM method was applied. The calculated pitch motions based on the NCEP-FNL Analyses wind input during June 15 generally overestimated the true pitch by 1-2°, respectively. The calculated pitch motion based on the WRF model wind input was most consistent with the observed pitch motion. The rapid change of pitch motion can be simulated in each method by using the 10-minute averaged value on ship's heading. Generally, the calculated pitch motions using EUT method is relatively higher than that using NSM method. Comparatively, use of the NSM method better captured the pitch motion during the rough weather event's increasing phase irrespective of wind inputs.

Figure 18 Comparison of observed and calculated pitch motions based on radar measurements and simulated wave hindcasts using EUT (top) and NSM (bottom) methods for Case 2.

Figure 19 compares the RMS of significant pitch amplitude using EUT and NSM methods, respectively for Case 2. Results based on the ERA-Interim and WRF model wind inputs give relatively small error, while NCEP-FNL wind inputs result in larger error. Similar to Case 1, when applying radar measurement, the error was largest since it failed to measure big waves.

Figure 19 Comparison of RMS of significant pitch amplitude using EUT and NSM methods for Case 2.

Figure 20 compares the calculated pitch frequency spectrums using EUT and NSM methods and based on radar measurements and wave hindcasts using the three different wind inputs with onboard observations at 12:00 on June 15. The calculated pitch frequency spectrums based on the simulated wave hindcasts were more consistent with observed pitch frequency spectrum at frequencies <0.5 rad/s than the calculated pitch frequency spectrum based on the radar measurement, which was much lower. EUT and NSM methods resulted in similar spectrum shapes. Similar to Case 1, the pitch frequency spectral peak calculated using EUT method was relative higher than the peak calculated using the NSM method, resulting in the relative higher pitch motion as shown previously in Figure 18.

Figure 20 Comparison of observed and calculated pitch frequency spectrums based on radar measurements and simulated wave hindcasts using EUT (left) and NSM (right) methods for Case 2 at 12:00 on June 15 2013.

4.2.3 Case 3: Tasman Sea (March 15–16)

Figure 21 compares the calculated pitch motion using EUT and NSM methods and based on wave hindcasts using the three different wind inputs with onboard observations for Case 3. The observation indicated that the pitch motion increased twice during March 15, and the calculated pitch motions reasonably replicated the two increasing of true pitch motion. However, all the calculated pitch motion during the beginning of March 15 underestimated the true pitch from 0.5° to 1°. During the end of March 15 (the second increasing of pitch motion), the calculated pitch

motions based on the NCEP-FNL Analyses was comparable with the observation. However, the calculated pitch motion based on the ERA-Interim was underestimated by approximately 1°. Conversely, the calculated pitch motion based on WRF model wind input was overestimated by approximately 2°. It is the reason why the simulated wave height is higher for 2 m in the WRF wind input than that in other methods, as shown in Figure 13. It implicates that the wind distribution computed on WRF model overestimates true winds than those on the linear interpolated wind inputs for this case. Similar to Case 1 and 2, the calculated pitch motion using EUT method was relatively higher than that using NSM method.

Figure 21 Comparison of observed and calculated pitch motions based on simulated wave hindcasts using EUT (top) and NSM (bottom) methods for Case 3.

Figure 22 compares the RMS of significant pitch amplitude using EUT and NSM methods, respectively for Case 3. Results based on the NCEP-FNL and ERA-Interim wind input give relatively small error, while WRF model wind inputs result in larger error since it overestimated pitch amplitude during the second increasing phase of pitch motion.

Figure 22 Comparison of RMS of significant pitch amplitude using EUT and NSM methods for Case 3.

To further investigate these differences, Figure 23 compares the calculated pitch frequency spectrums using EUT and NSM methods and based on wave hindcasts using the three different wind inputs with onboard observations at 3:00 on March 15. Similar to Case 1 and 2, the calculated pitch frequency spectrums based on the simulated wave hindcasts were more concentrated in the lower frequency bands. Use of the both EUT and NSM method resulted in overestimation of the

true pitch frequency spectrums between frequencies of 0.45-0.65 rad/s, and underestimation of the true pitch frequency spectrums at frequencies > 0.65 rad/s. Using either method, the calculated pitch frequency spectrum was general relatively low based on the WRF Model wind input, consistent with its lower pitch motion peak shown previously in Fig. 20. Similar to Case 1 and 2, the pitch frequency spectrum calculated using EUT method was relative higher than the peak calculated using the NSM method.

Figure 23 Comparison of observed and calculated pitch frequency spectrums based on simulated wave hindcasts using EUT (left) and NSM (right) methods for Case 3 at 3:00 on March 15 2013.

5. Conclusions

In this study, we simulated wave hindcasts using NCEP-FNL Analyses, ERA-Interim, and WRF Model wind inputs with various spatial and temporal resolutions for three cases of rough-sea navigation in the Southern Hemisphere. The simulated waves were validated using onboard ship motion measurements. Comparisons of the observed and calculated pitch motions indicated that the simulated wave hindcasts reasonably replicated rough waves, suggesting potential application to ship weather routing under severe weather conditions.

Wind speed comparisons indicated that, for relatively high wind speeds, each of the simulation models based on the three different wind input sources tended to underestimate the true wind speeds by up to approximately 10 m/s. Wind speed estimates based on the ERA-Interim wind input were consistently lower than the estimates based on the NCEP-FNL Analyses wind input. The increased spatial and temporal resolutions offered by the WRF Model wind input tended to improve the accuracy of wind speed estimates and provided greater detail regarding wind speed variation.

Corresponding to the wind speed, the simulated waves using the NCEP-FNL Analyses wind input were generally higher than the waves estimated using the ERA-Interim wind input, and consequently generated more violent ship motion. This result is consistent with other study findings (e.g. Campos and Guedes Soares, 2016). Results also indicated that the simulated waves using the higher-resolution WRF Model wind input both overestimated and underestimated the wave height and ship motion, depending on the case. Increased spatial resolution of WW3 model can improve estimation accuracy.

The calculation of pitch motions in rough weather events is sensitivity to relative wave direction. Supplemental investigations confirmed that average of ship direction measurement every 1 hour is not appropriate for the calculation of pitch motions using wave hindcasts when ship course changes frequently under the rough sea condition. Average of ship direction by shorter time interval such as 10 min is better in such cases.

In conclusion, by using onboard ship motion measurements, we have effectively validated efforts to simulate rough waves in the Southern Hemisphere. The results suggest that near-surface winds from the ERA-Interim generally underestimated rough waves, while those from the NCEP-FNL Analyses had a contrary tendency. In addition, although the wind inputs from the ERA-Interim produced simulated wave hindcasts more consistent with measured results, these same inputs generally underestimated the increasing-phase pitch motion under severe weather conditions, which poses a danger for ships. Thus, the use of wind inputs from the NCEP-FNL Analyses or higher-resolution WRF Model is recommended for application to ship weather routing systems under severe weather conditions in the Southern Hemisphere.

Acknowledgement

We appreciate the assistance of Shoei Kisen Kaisha Ltd., Northstar Shipping Management Ltd., the bulk carrier's crew, and shipping agents in Singapore and Australia in conducting this study. In

addition, we would like to thank Mr. Keiichi Hirayama, Japan Radio Ltd., for his advice on radar wave measurement. This study was sponsored by the Japan Society for the Promotion of Science (JSPS) through its Grants-in-Aid for Scientific Research (Scientific Research B) program titled "A new optimum shipping system integrated with safety, economy, and ocean environment for international maritime shipping" (No. 25282103) and the Fundamental Research Developing Association for Shipbuilding and Offshore (REDAS) titled "Accurate estimation of wave spectrum and ship performance in rough seas in the Southern Hemisphere using two step validations of sea clutter of Radar" (REDAS16-4(7)).

References

Alves, J.-H.G.M., "Numerical modeling of ocean swell contributions to the global wind-wave climate", *J. Ocean Modelling* 11, pp.98–122, 2006.

Bosserelle, C., Pattiaratchi, C., and Haigh, I., "Inter-annual variability and longer-term changes in the wave climate of Western Australia between 1970 and 2009", *J. Ocean Dynamics, Vol.62*, pp.63–76, 2012.

Bowditch, N., "The American Practical Navigator: an epitome of navigation", *National Imagery and Mapping Agency*, *Paradise Cay Publications,* p.896, 2002.

Campos, R.M. and Guedes Soares, C., "Comparison of HIPOCAS and ERA wind and wave reanalyses in the North Atlantic Ocean", *J. Ocean Engineering* Vol.112, pp.320–334, 2016.

Cavaleri, L. and Malanotte-Rizzoli, P., "Wind-wave prediction in shallow water: theory and applications," *Journal of Geophysical Research*, *Vol.86*, pp.10961–10973, 1981.

Cavalieri, D.J., Parkinson, C.L., Gloersen, P., and Zwally, H.J. (Updated annually). "Sea Ice Concentrations from Nimbus-7 SMMR and DMSP SSM/I-SSMIS Passive Microwave Data, Version 1. Boulder, Colorado, United States", *NASA National Snow and Ice Center Distributed Active Archive Center*, Doi: http://dx.doi.org/10.5067/8GQ8LZQVLOVL, 1996.

Chen, H., "A dynamic program for minimum cost ship routing under uncertainty", *Ph.D. Thesis*, *Department of Ocean Engineering, Massachusetts Institute of Technology*, *Cambridge*, *Massachusetts*, 1978.

Delitala, A.M.S., Gallino, S., Villa, L., Lagouvardos, K., and Drago, A., "Weather routing in long-distance Mediterranean routes", *Theoretical and Applied Climatology*, *Vol.102*, pp.125–137, 2010.

Dee, D. P., Uppala, S. M., Simmons, A. J., Berrisford, P., Poli, P., Kobayashi, S., Andrae, U., Balmaseda, M. A., Balsamo, G., Bauer, P., Bechtold, P., Beljaars, A. C. M., van de Berg, L., Bidlot, J., Bormann, N., Delsol, C., Dragani, R., Fuentes, M., Geer, A. J., Haimberger, L., Healy, S. B., Hersbach, H., Hólm, E. V., Isaksen, L., Kållberg, P., Köhler, M., Matricardi, M., McNally, A. P., Monge-Sanz, B. M., Morcrette, J.-J., Park, B.-K., Peubey, C., de Rosnay, P., Tavolato, C., Thépaut, J.-N., and Vitart, F., "The ERA-Interim reanalysis: configuration and performance of the data assimilation system", *Quarterly Journal of the Royal Meteorological Society*, Vol.137, pp.553–597, doi: 10.1002/qj.828, 2011

Dudhia, J., "Numerical study of convection observed during the winter monsoon experiment using a mesoscale two-dimensional model", *Journal of the Atmospheric Sciences*, *Vol.46*, *No.20*, pp. 3077–3107, 1989.

Durrant T., Greenslade, D., Hemer, M., and Trenham, C., "A global wave hindcast focused on the central and south Pacific", *Collaboration for Australian Weather and Climate Research (CAWCR) Technical Report*, *No. 070*, p. 45, 2014.

Feng, H., Vandermark, D., Quilfen, Y., Chapron, B., and Beckley, B., "Assessment of wind-forcing impact on a global wind-wave model using the TOPEX altimeter", *J. Ocean Engineering Vol.33*, *No.11-12,* pp.1431–1461, 2006.

Gorman, R.M., Bryan, K.R., and Laing, A.K., "Wave hindcast for the New Zealand region: Deep-water wave climate", *New Zealand Journal of Marine and Freshwater Research*, *Vol.37*, pp.589–612, 2003.

Hagiwara, H. and Spaans, J.A., "Practical weather routing of sail-assisted motor vessels", *Journal of Navigation*, *Vol.40*, *No.1*, pp.96–119, 1987.

Hasselmann, K., Barnett, T.P., Bouws, E., Carlson, H., Cartwright, D.E., Enke, K., Ewing, J.A., Gienapp, H., Hasselmann, D.E., Kruseman, P., Meerburg, A., Müller, P., Olbers, D.J., Richter, K., Sell, W., and Walden, H., "Measurements of wind-wave growth and swell decay during the Joint North Sea Wave Project (JONSWAP)", *Ergänzungsheft zur Deutschen Hydrographischen Zeitschrift, Reihe,* A(8)12, p. 95, 1973.

Hasselmann, S., Hasselmann, K., Allender, J.H., and Barnett, T.P., "Computations and parameterizations of the nonlinear energy transfer in a gravity-wave spectrum, Part II: parameterizations of the nonlinear energy transfer for application in wave models", *Journal of Physical Oceanography*, *Vol.15*, pp.1378–1391, 1985.

Hinnenthal, J., "Robust Pareto – Optimum Routing of Ships utilizing Deterministic and Ensemble Weather Forecasts", *Ph.D. Thesis, Berlin University of Technology*, p. 133, 2008.

Hong, S.-Y., Dudhia, J., and Chen, S.-H, "A revised approach to ice microphysical processes for the bulk parameterization of clouds and precipitation", *Monthly Weather Review*, *Vol.132*, *No.1*, pp. 103–132, 2004.

Hong, S.-Y., Noh, Y., and Dudhia, J., "A new vertical diffusion package with an explicit treatment of entrainment processes", *Monthly Weather Review*, *Vol.134*, *No.9*, pp.2318–2341, 2006.

James, R.W., "Application of Wave Forecasts to Marine Navigation", *U.S. Naval Oceanographic Office*, *Naval Science and Technological Laboratory (NSTL)*, 1957.

Kain, J.S., "The Kain-Fritsch convective parameterization: an update", *Journal of Applied Metrotology*, *Vol.43*, *No.1*, pp.170–181, 2004.

Kashiwagi, M., "Numerical seakeeping calculations based on the slender ship theory", *J. Ship Technology Research*, *Vol.44*, *No.4*, pp.167–192, 1997.

Lin, Y.-H., Fang, M.-C., and Yeung, R.W., "The optimization of ship weather-routing algorithm based on the composite influence of multi-dynamic elements", *J. Applied Ocean Research*, *Vol.43*, pp.184–194, 2013.

Michalakes, J., Dudhia, J., Gill, D., Henderson, T., Klemp, J., Skamarock, W., and Wang, W., "The weather research and forecast model: software architecture and performance", *Proceedings of the 11th ECMWF Workshop on the Use of High Perfomance Computing in Meteorology*, pp.25–29 October 2004, Reading, U.K., Ed. George Mozdzynski, 2004.

Mlawer, E.J., Taubman, S.J., Brown, P.D., Iacono, M.J., and Clough, S.A., "Radiative transfer for inhomogeneous atmospheres: RRTM, a validated correlated-k model for the longwave", *Journal of Geophysical Research Vol.102*, *D14*, pp.16663–16682, 1997.

Nielsen, U.D., "The wave buoy analogy–estimating high-frequency wave excitations", *J. Applied Ocean Research*, *Vol.30*, pp.100–106, 2008.

National Oceanic and Atmospheric Administration (NOAA), "National Geophysical Data Center, Etopo2v2 global gridded 2-minute database", 2006.

National Centers for Environmental Prediction/National Weather Service/NOAA/U.S. Department of Commerce, "NCEP FNL Operational Model Global Tropospheric Analyses, continuing from July 1999", *Research Data Archive at the National Center for Atmospheric Research*, *Computational and Information Systems Laboratory*. https://doi.org/10.5065/D6M043C6, 2000 (updated daily)

Padhy, C.P., Sen, D., and Bhaskaran, P.K., "Application of wave model for weather routing of ships in the North Indian Ocean", *Natural Hazards*, *Vol.44*, pp.373–385, 2008.

Prpić-Oršić, J. and Faltinsen, O.M., "Estimation of ship speed loss and associated CO_2 emissions in a seaway", *J. Ocean Engineering*, *Vol.44*, pp.1–10, 2012.

Qinetiq, Lloyd's Register Group Limited, and the University of Strathclyde, "Global Marine Trends 2030", 2013.

Rapizo, H., Babanin, A.V., Schulz, E., Hemer, M.A., and Durrant, T.H., "Observation of wind-waves from a moored buoy in the Southern Ocean", *J. Ocean Dynamics*, *Vol.65*, pp.1275–1288, 2015.

Salvesen, N., Tuck, E.O., and Faltinsen, O., "Ship motions and sea loads", *Proceedings of the Society of Naval Architects and Marine Engineers*, Vol,78, pp.250–287, 1970.

Sasa, K., Terada, D., Shiotani, S., Wakabayashi, N., Ikebuchi, T., Chen, C., Takayama, A., and Uchida, M., "Evaluation of ship performance in international maritime transportation using an onboard measurement system–in case of a bulk carrier in international voyages", *J. Ocean Engineering*, *Vol.104*, pp.294–309, 2015.

Sasaki, W., "Impact of satellite data assimilation in atmospheric reanalysis on the marine wind and wave climate", *Journal of Climate*, *Vol.29*, pp.6351–6361, 2016.

Sen, D. and Padhy, C.P., "An approach for development of a ship routing algorithm for application in the North Indian Ocean region", *J. Applied Ocean Research*, *Vol.50*, pp.173–191, 2015.

Smith, S.D., "Coefficients for sea surface wind stress, heat flux and wind profiles as a function of speed and temperature", *Journal of Geographic Research*, *Vol.93*, *No. C12*, pp.467-472, 1988.

Smith, T.W.P., Jalkanen, J.P., Anderson, B.A., Corbett, J.J., Faber, J., Hanayama, S., O'Keeffe, E., Parker, S., Johansson, L., Aldous, L., Raucci, C., Traut, M., Ettinger, S., Nelissen, D., Lee, D.S., Ng, S., Agrawal, A., Winebrake, J.J., Hoen, M., Chesworth, S., and Pandey, A., "Third IMO Greenhouse Gas Study 2014"*, International Maritime Organization (IMO)*, June 2014, p. 328, 2014.

Storm, B., Dudhia, J., Basu, S., Swift, A., and Giammanco, I., "Evaluation of the weather research and forecasting model on forecasting low-level jets: implications for wind energy". *Wind Energy*, *Vol.12*, *No.1*, pp.81–90. DOI: 10.1002/we.288, 2008.

Stopa, J.E., Ardhuin, F., Babanin, A., and Zieger, S., "Comparison and validation of physical wave parameterizations in spectral wave models", *J. Ocean Modelling*, *Vol.103*, pp.2–17, 2016.

Stopa, J.E. and Cheung, K.F., "Intercomparison of wind and wave data from the ECMWF Reanalysis Interim and the NCEP Climate Forecast System Reanalysis", *J. Ocean Modelling*, *Vol.75*, pp.65–83, 2014.

Shao, W., Zhou, P., and Thong, S.K., "Development of a novel forward dynamic programming method for weather routing", *Journal of Marine Science and Technology*, *Vol.17*, *No.2*, pp.239–251, 2012.

Takashima, K., Mezaoui, B., and Shoji, R., "On the fuel saving operation for coastal merchant ships using weather routing", *International Journal on Marine Navigation and Safety of Sea Transportation*, *Vol.3*, *No.4*, pp.401–406, 2009.

Tolman, H.L., "Effects of numerics on the physics in a third-generation wind-wave model", *Journal of Physical Oceanography*, *Vol.22*, pp.1095–1111, 1992.

Tolman, H.L., Balasubramaniyan, B., Burroughs, L.D., Chalikov, D.V., Chao, Y.Y., Chen, H.S., and Gerald, V.M., "Development and implementation of wind-generated ocean surface wave models at NCEP", *Weather and Forecasting*, *Vol.17*, pp.311–333, 2002.

Tolman, H.L., "User manual and system documentation of WAVEWATCH III, version 4.18", *National Oceanic and Atmospheric Administration/National Weather Service/National Centers for Environmental Prediction (NOAA/NWS/NCEP) Technical Note*, p.282, 2014.

Tolman, H.L. and Chalikov, D., "Source terms in a third-generation wind wave model", *Journal of Physical Oceanography*, *Vol.26*, pp.2497–2518, 1996.

United Nations Conference on Trade and Development (UNCTAD), "Review of Maritime Transport 2016", *UNCTAD/Review of Maritime Transport (RMT) 2016*, *United Nations Conference on Trade and Development*, *Geneva*, *Switzerland*, p. 104, 2016.

Vettor, R. and Guedes Soares, C., "Rough weather avoidance effect on the wave climate experienced by oceangoing vessels", *J. Applied Ocean Research*, *Vol.59*, pp.606–615, 2016.

Watson, L.R. and Bauman III, W.H., "Weather Research and Forecasting Model Wind Sensitivity Study at Edwards Air Force Base, CA", *National Aeronautics and Space Administration Contractor Report, NASA/CR-2008-214755*, 2008.

Figure 1

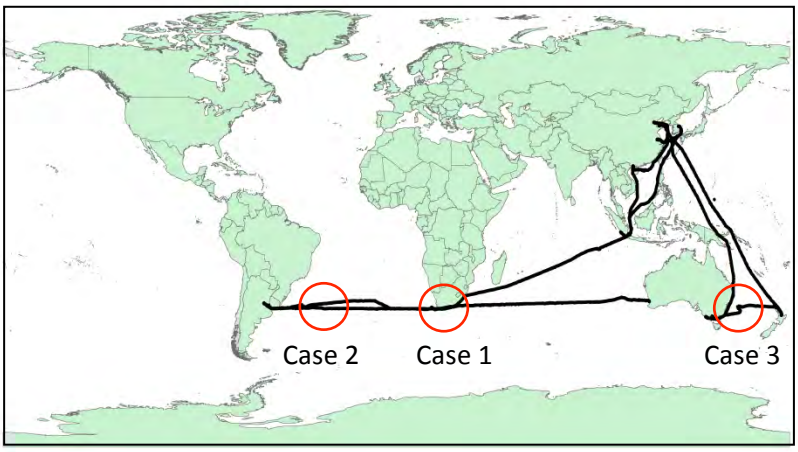

Figure 1 Rough-sea navigation cases considered in this study (black lines indicate ship routes; red circles indicate three rough weather events).

Figure 2

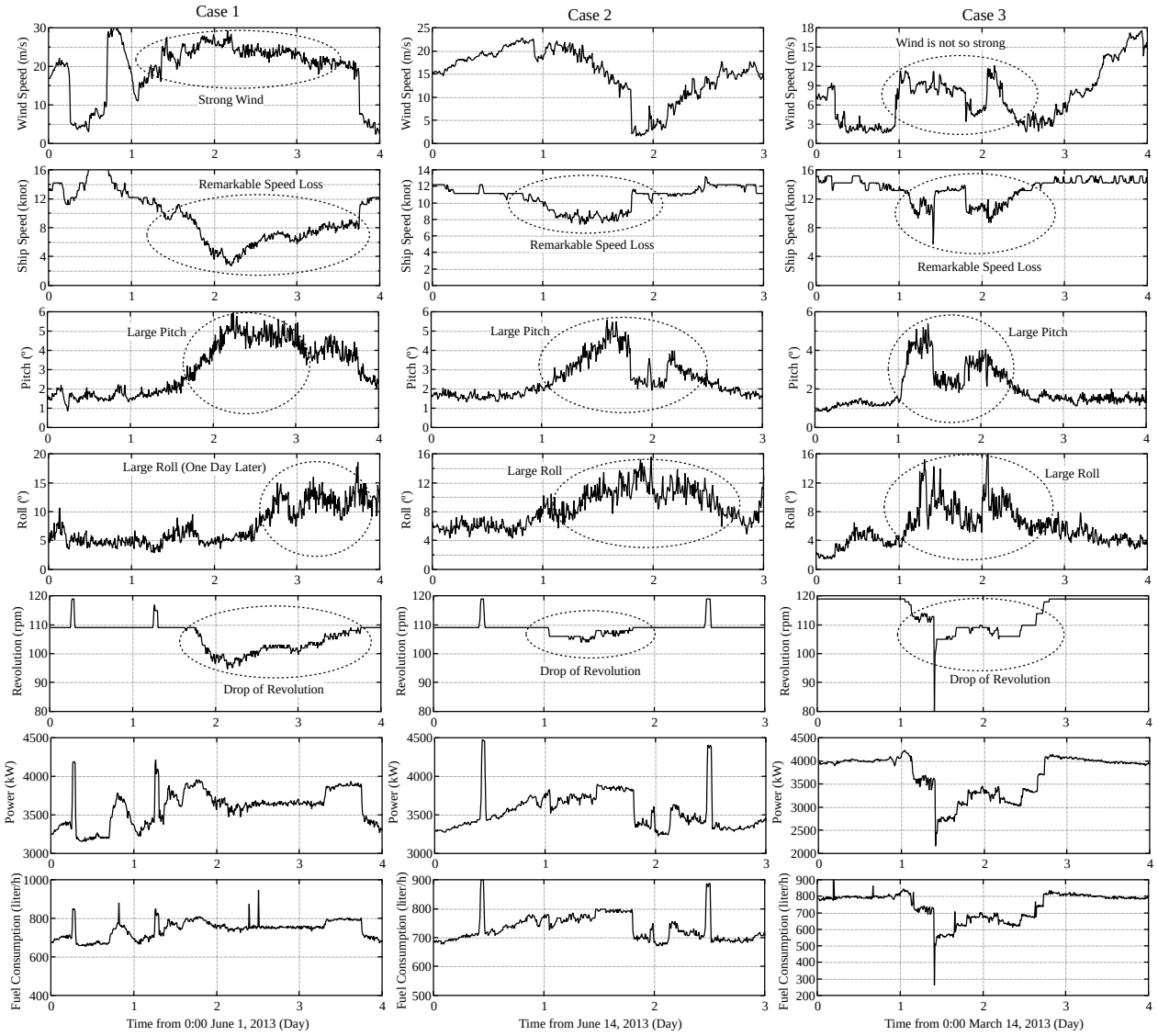

Figure 2 Measured data for Cases 1, 2, and 3: (a) wind speed, (b) ship speed, (c) pitch motion, (d) roll motion, (e) engine shaft revolution, (f) engine power, and (g) fuel consumption [note that the observed spikes in Cases 1 and 2 (e–g) are attributable to regular daily maintenance of engine].

Figure 3

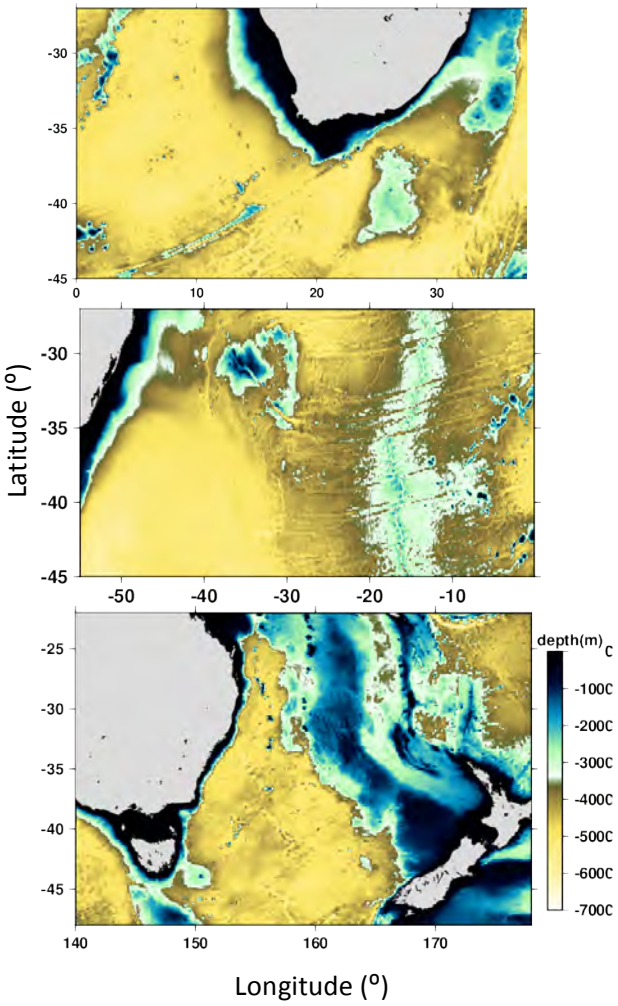

Figure 3 Bathymetry and computational domain for cases 1, 2, and 3.

Figure 4

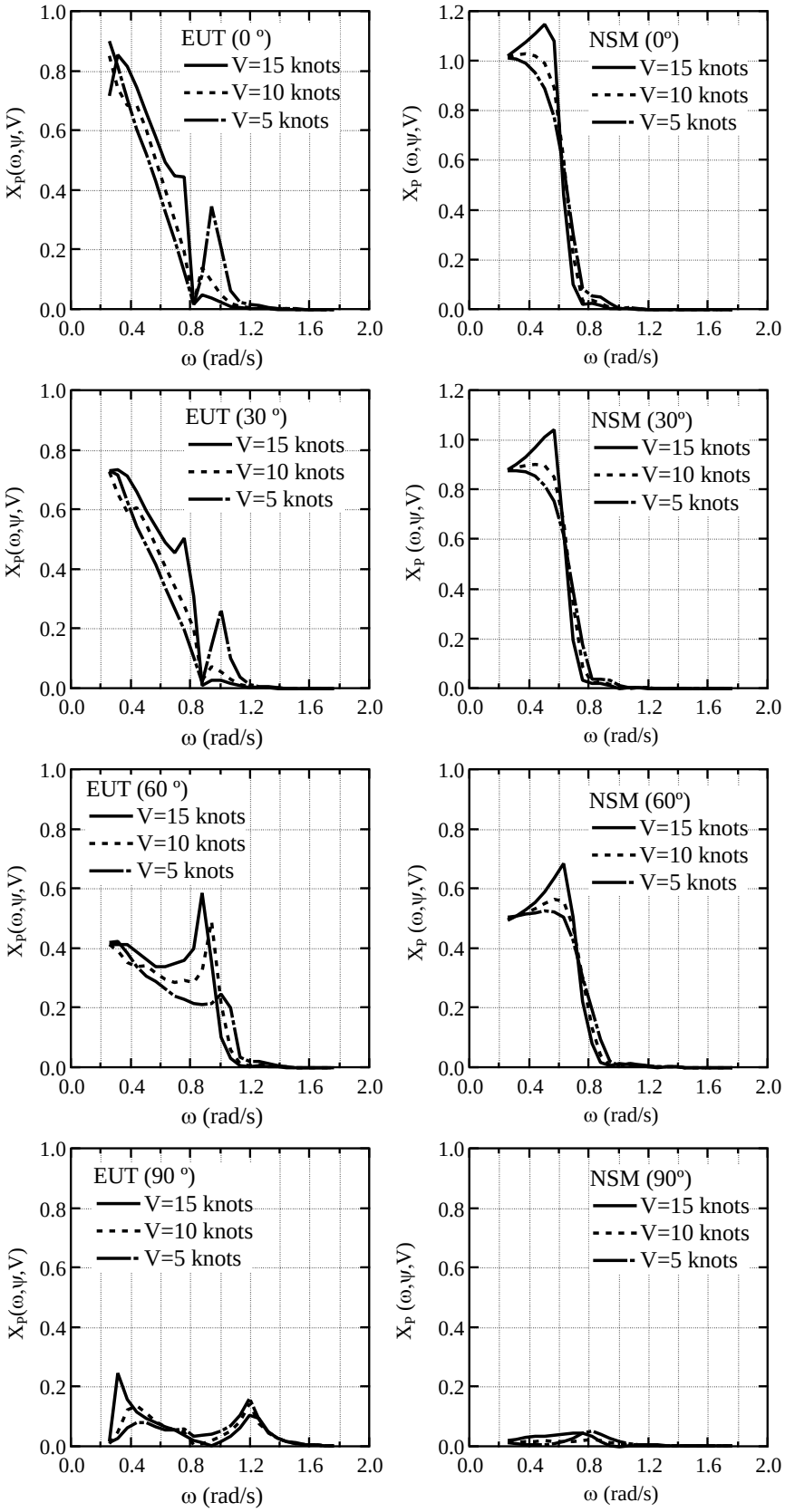

Figure 4 Computed results of frequency response functions of pitch motion (Case 1 and 2, 0-90°)

Figure 5

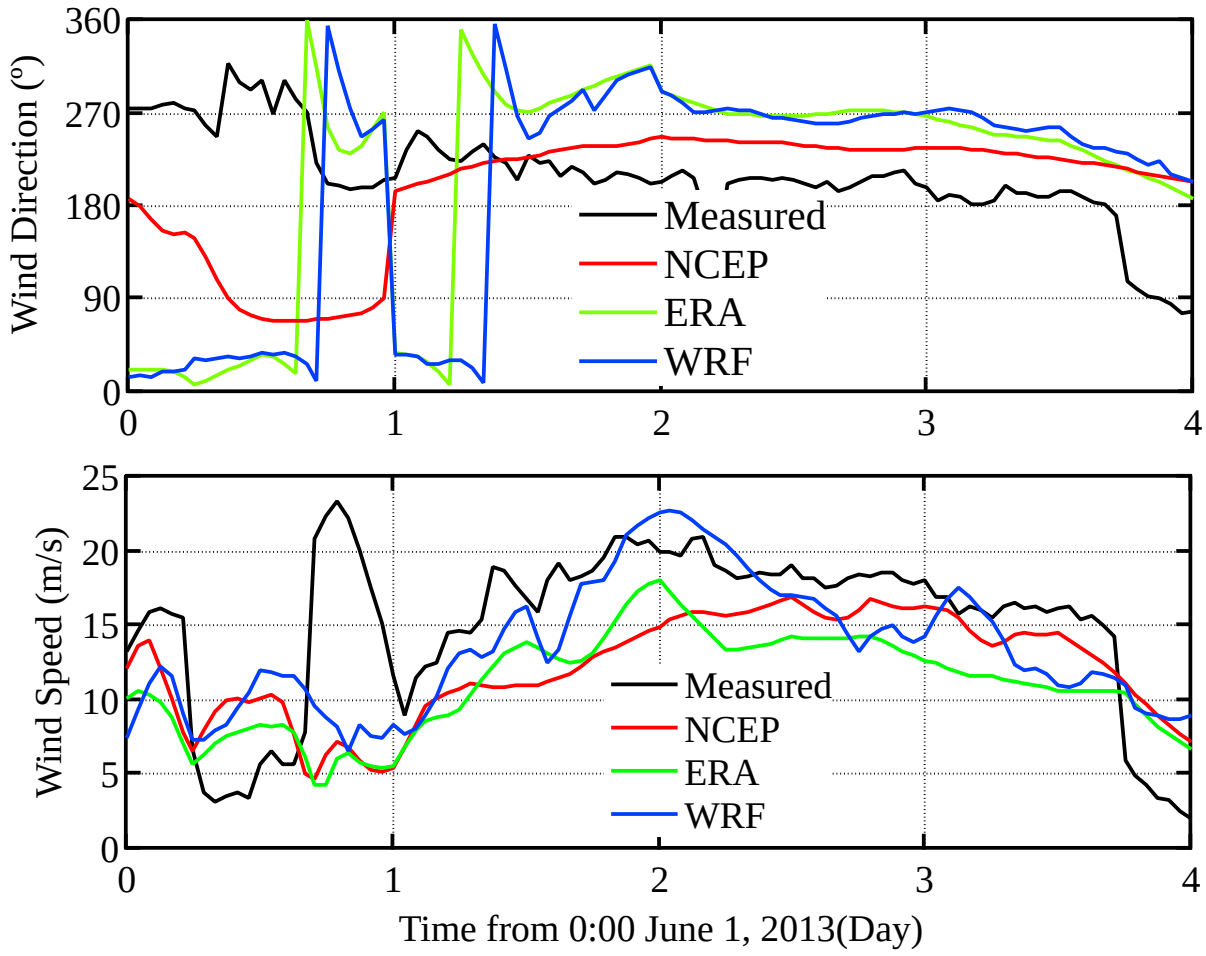

Figure 5 Comparison of observed and simulated wind directions and speeds for Case 1.

Figure 6

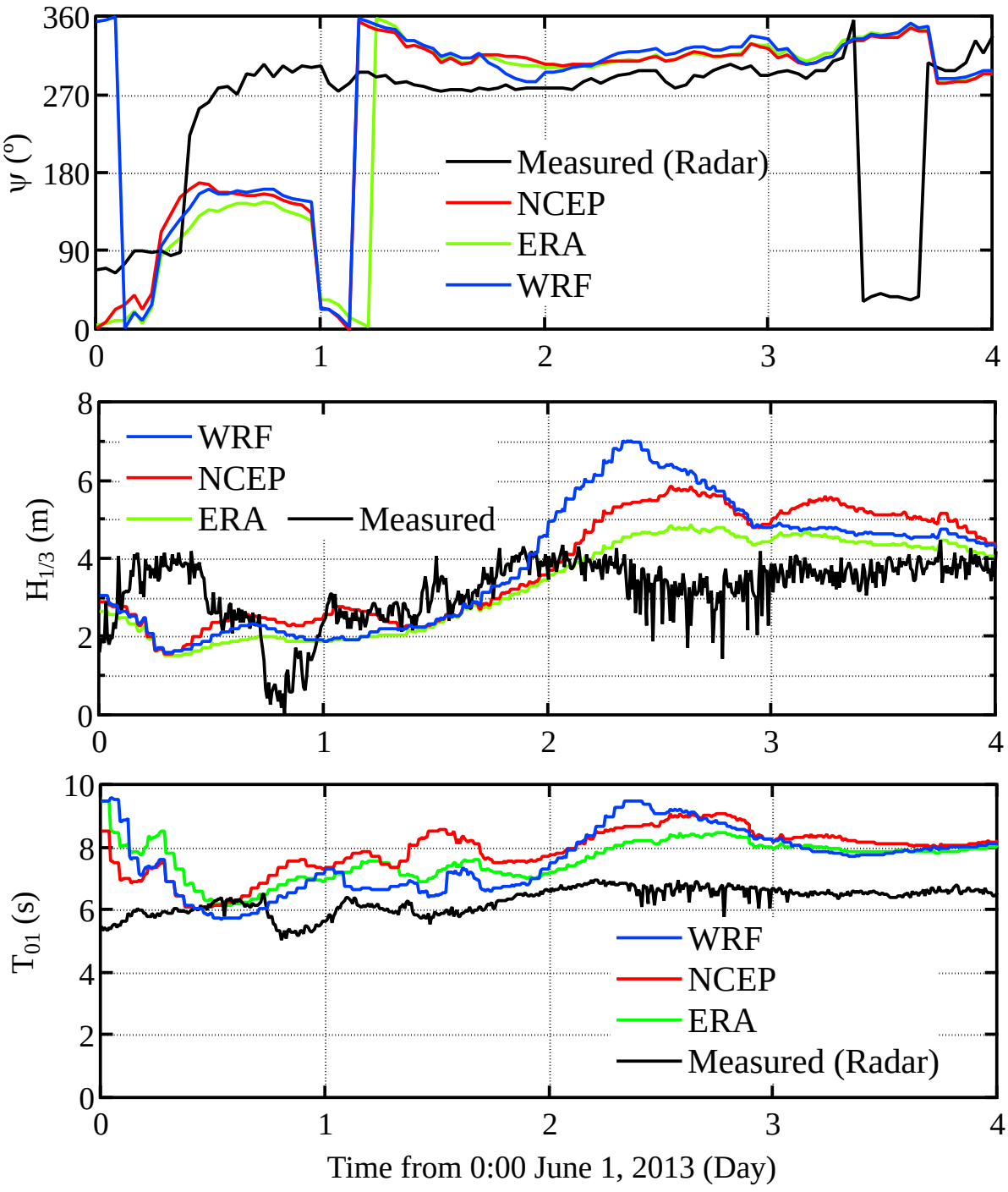

Figure 6 Comparison of observed and simulated wave directions, significant wave heights and wave periods for Case 1.

Figure 7

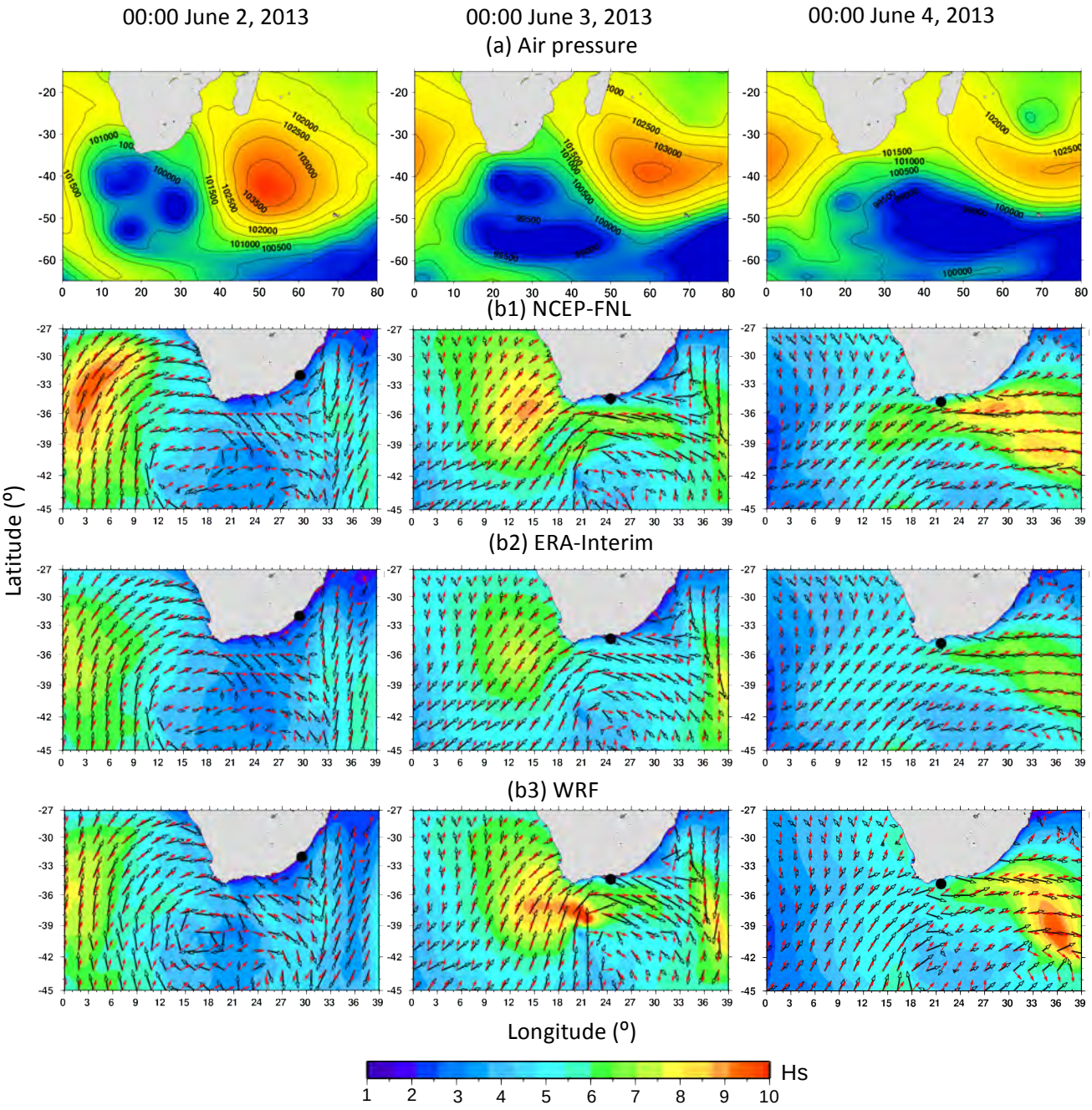

Figure 7 Snapshot sea level pressure distributions and comparative simulated wave fields for Case 1 (shaded areas denote significant wave height, red arrows denote wave direction, black arrows denote wind vector, and black dot denote the ship position).

Figure 8

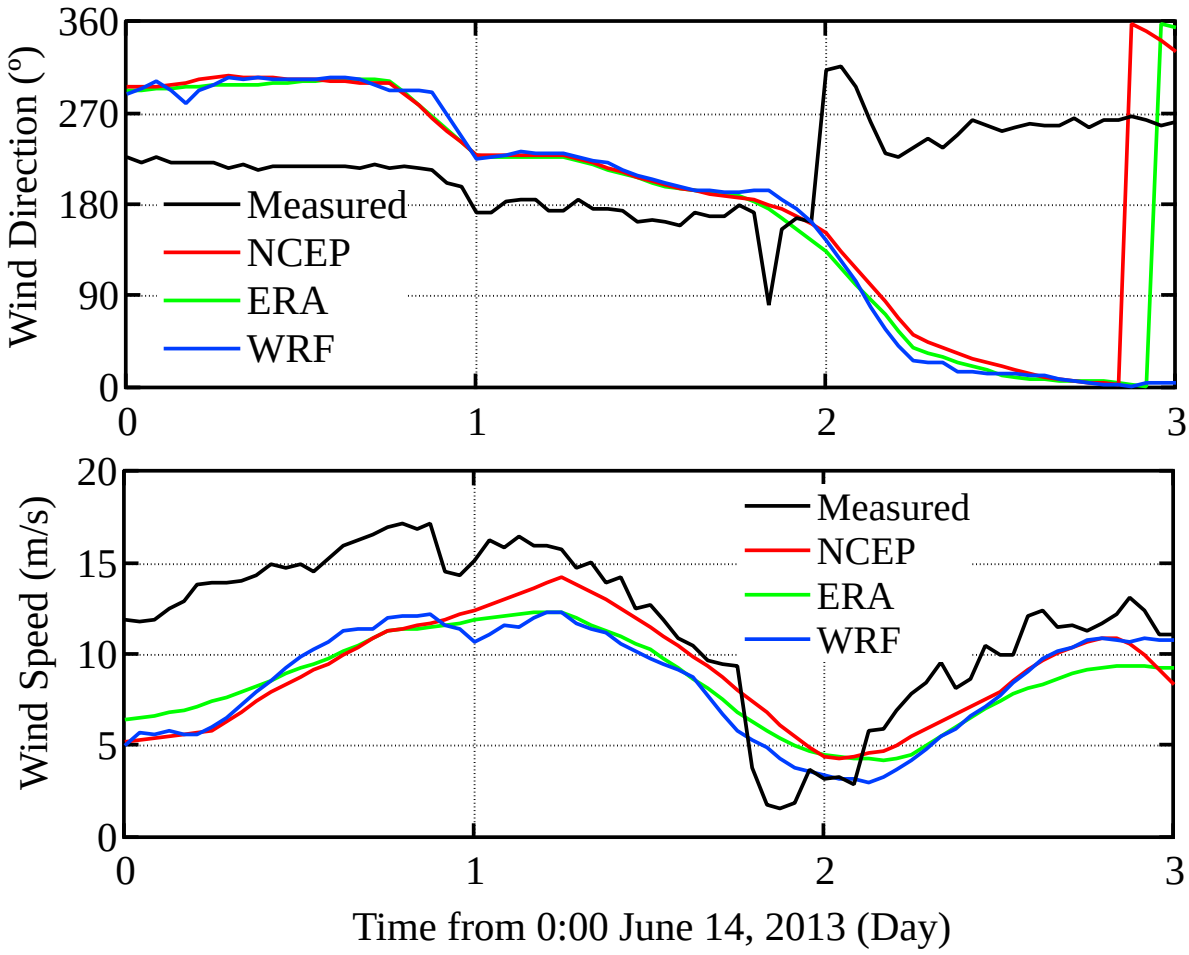

Figure 8 Comparison of observed and simulated wind directions and speeds for Case 2.

Figure 9

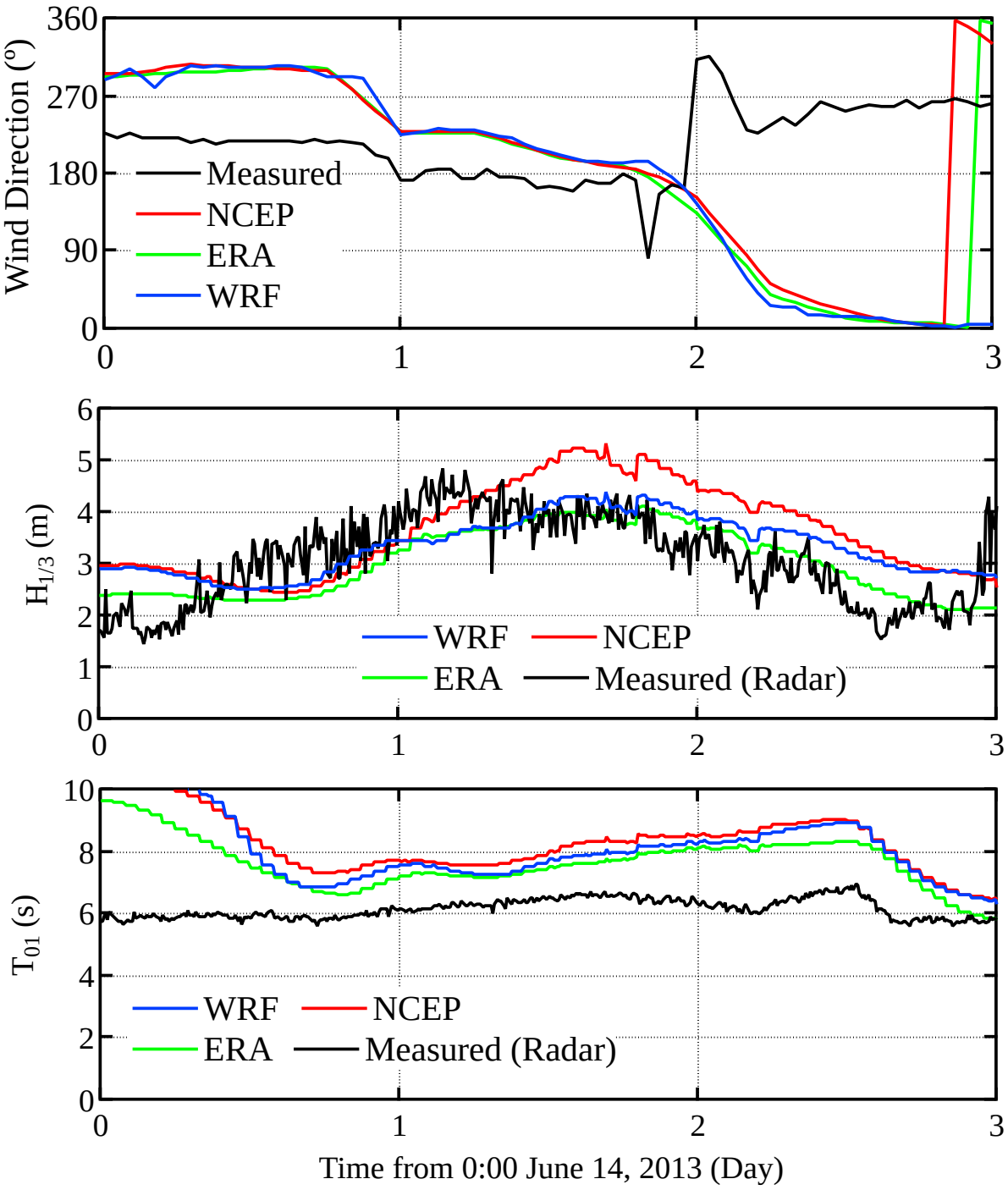

Figure 9 Comparison of observed and simulated wave directions, significant wave heights and wave periods for Case 2.

Figure 10

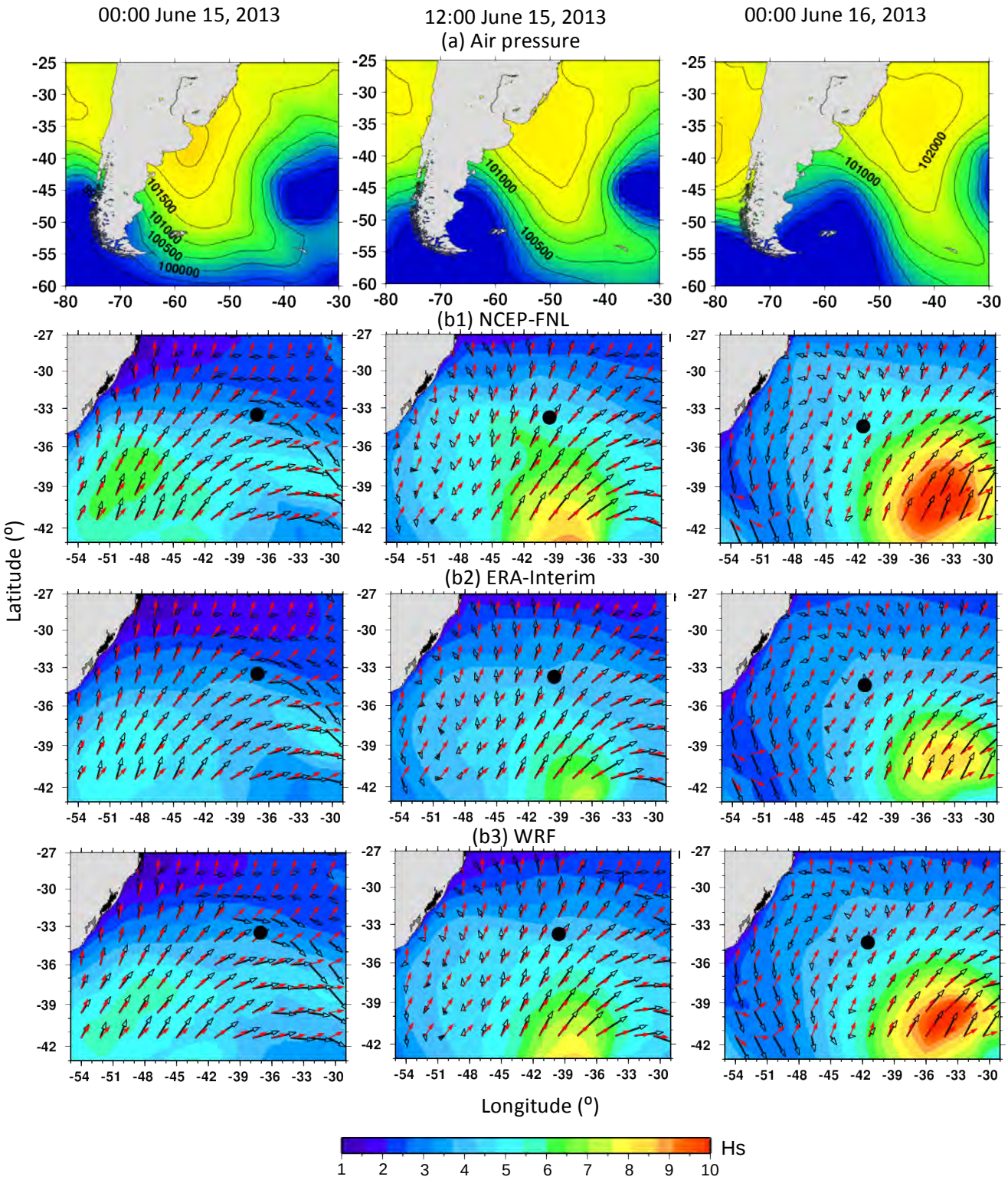

Figure 10 Snapshot sea level pressure distributions and comparative simulated wave fields for Case 2 (shaded areas denote significant wave height, red arrows denote wave direction, black arrows denote wind vector, and black dot denote the ship position).

Figure 11

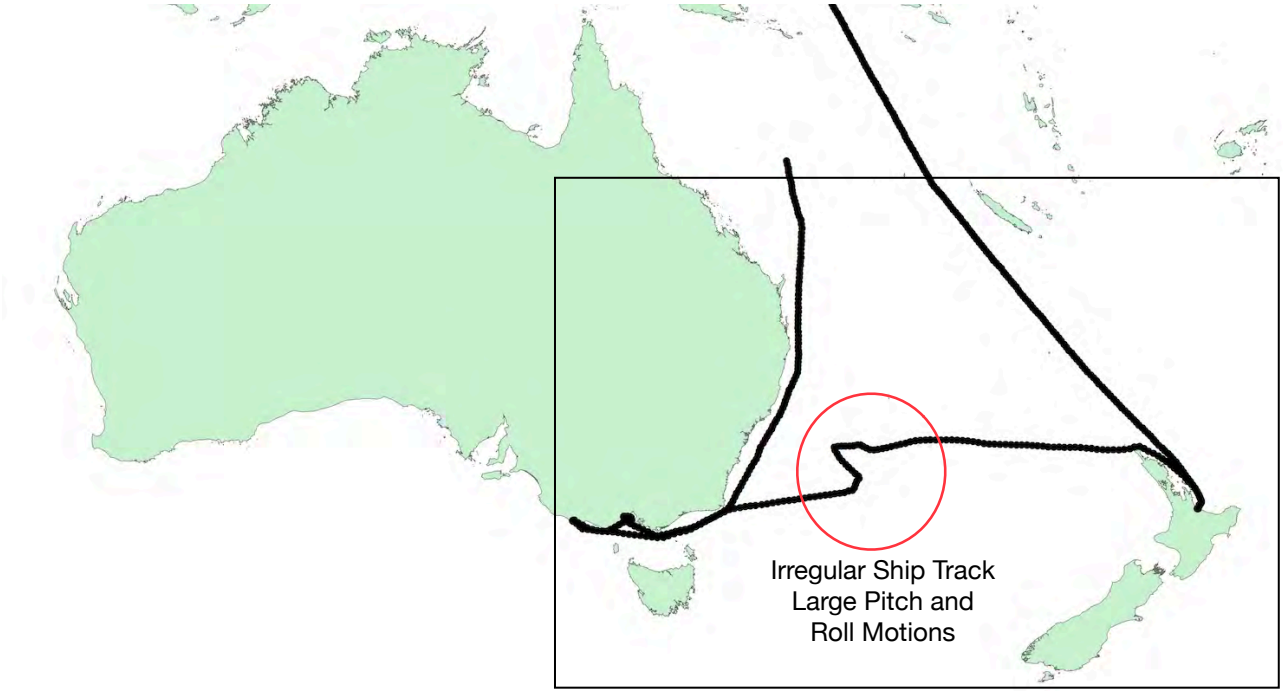

Figure 11 Ship track in mid-March 2013.

Figure 12

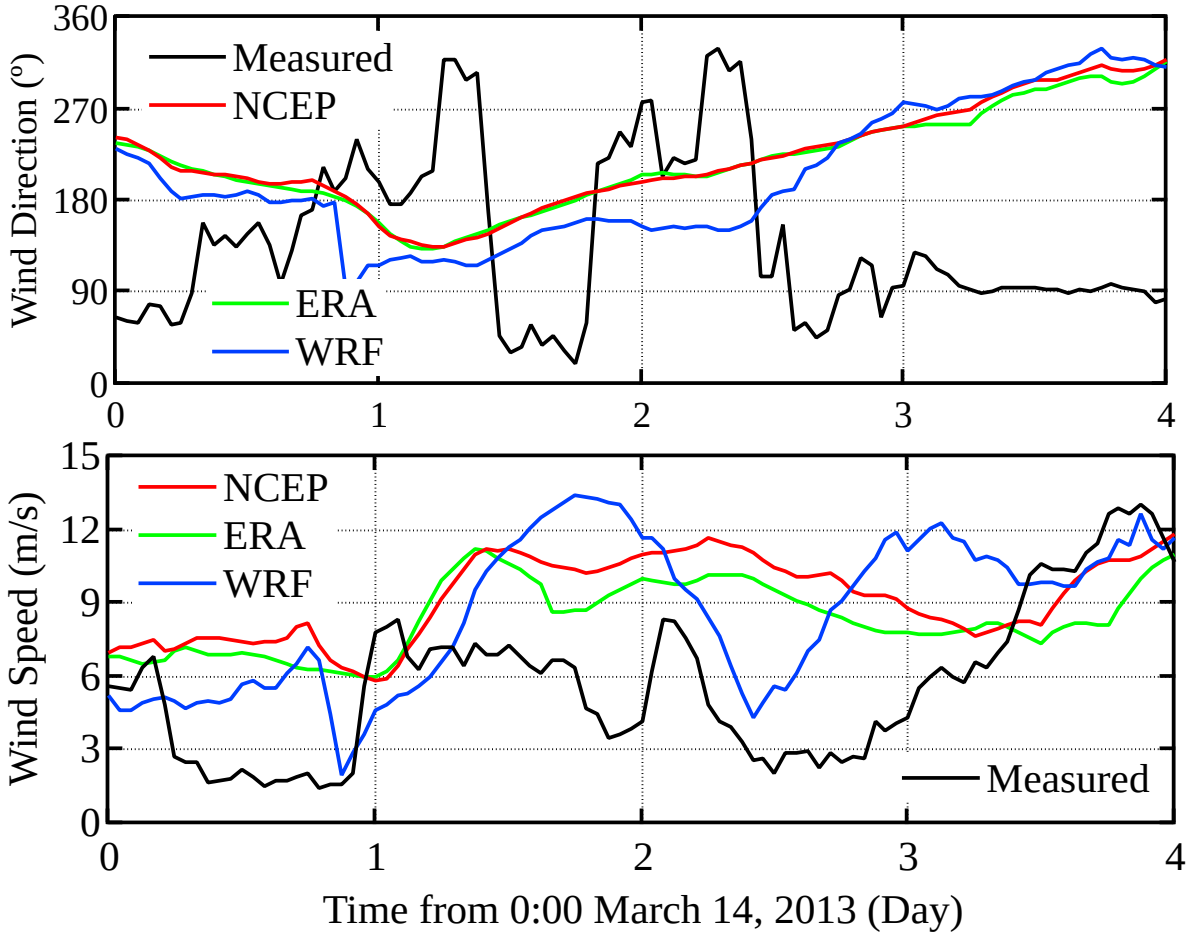

Figure 12 Comparison of observed and simulated wind speeds for Case 3.

Figure 13

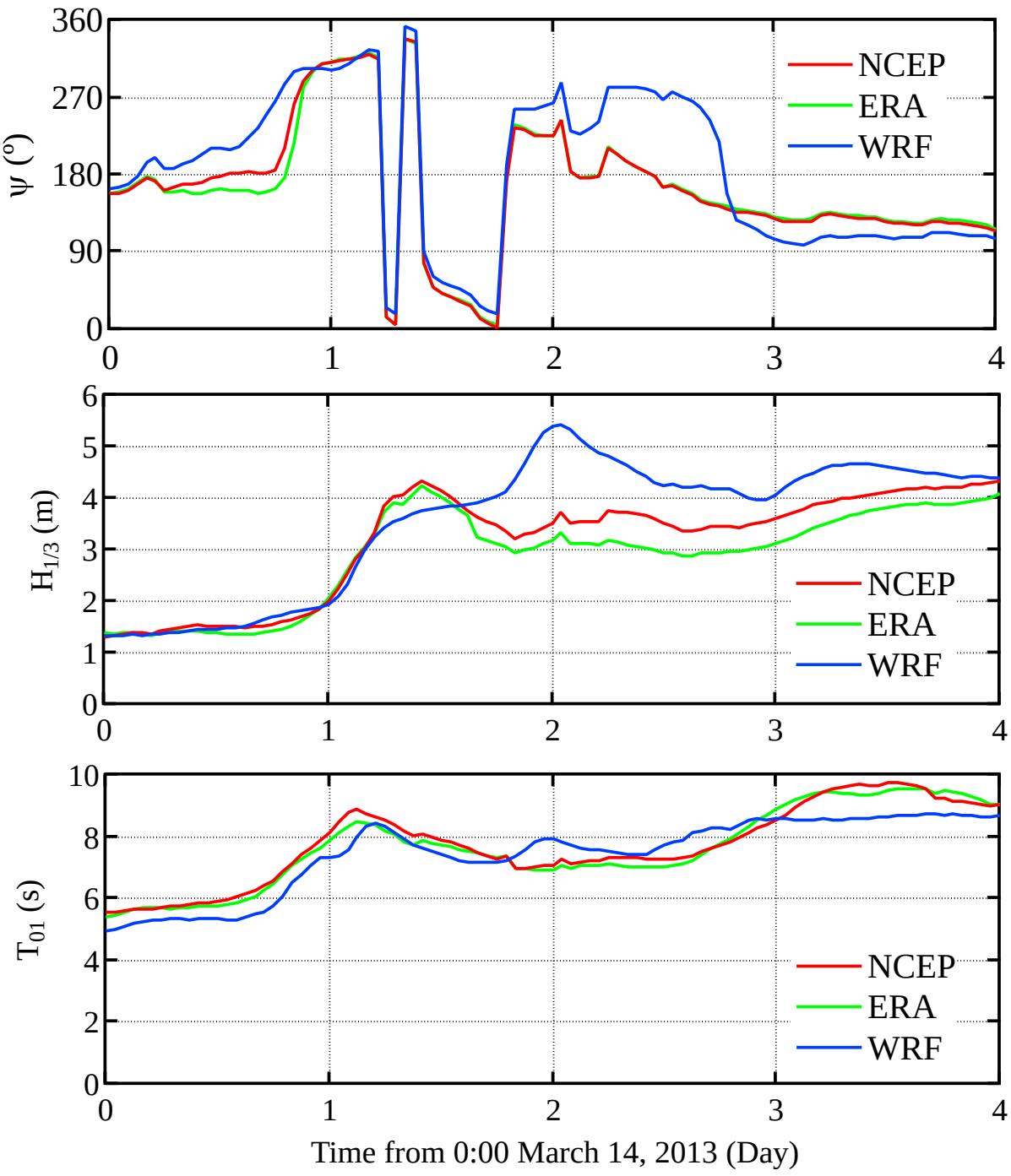

Figure 13 Comparison of simulated significant wave heights for Case 3.

Figure 14

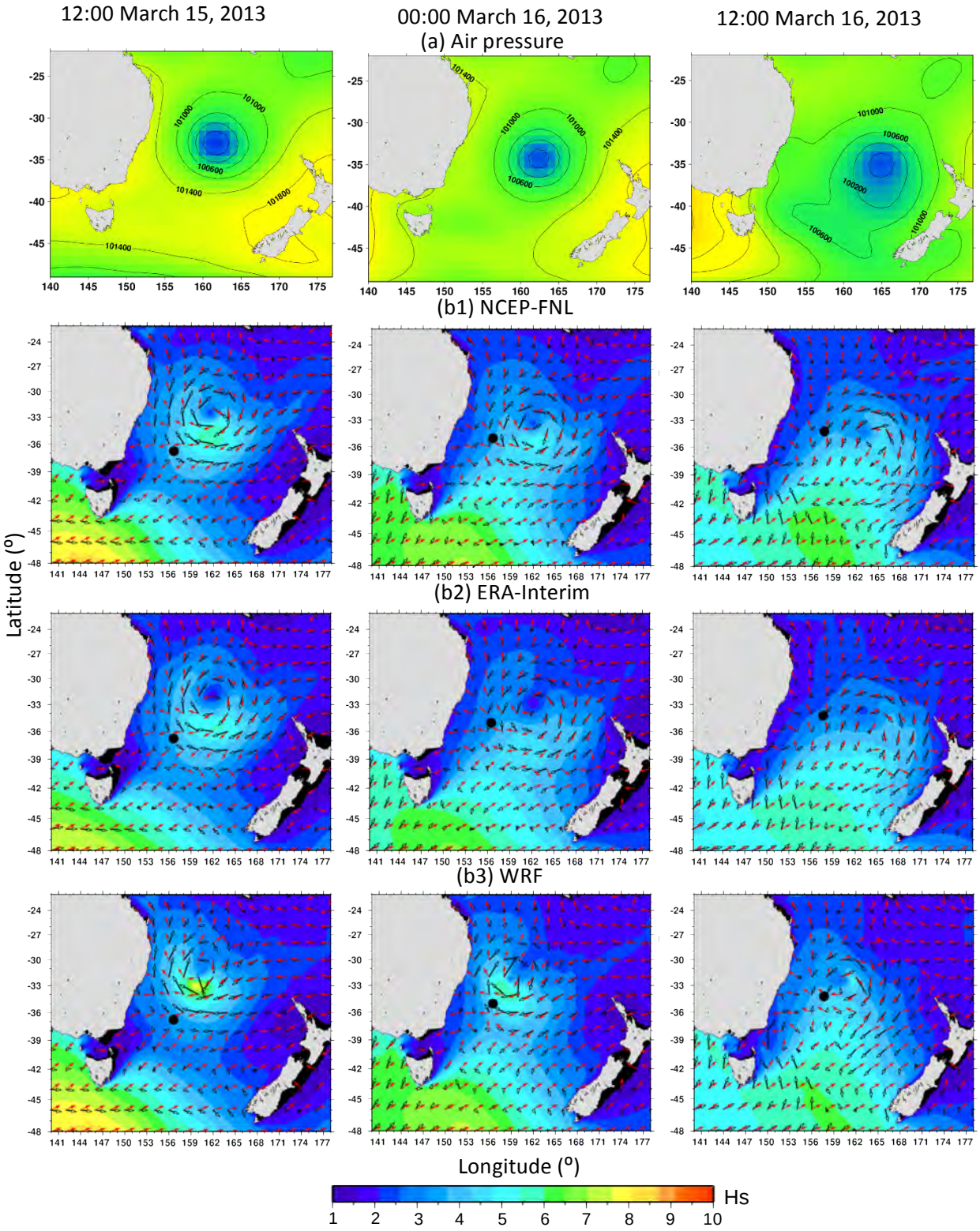

Figure 14 Snapshot sea level pressure distributions and comparative simulated wave fields for Case 3 (shaded areas denote significant wave height, red arrows denote wave direction, black arrows denote wind vector, and black dot denote the ship position).

Figure 15

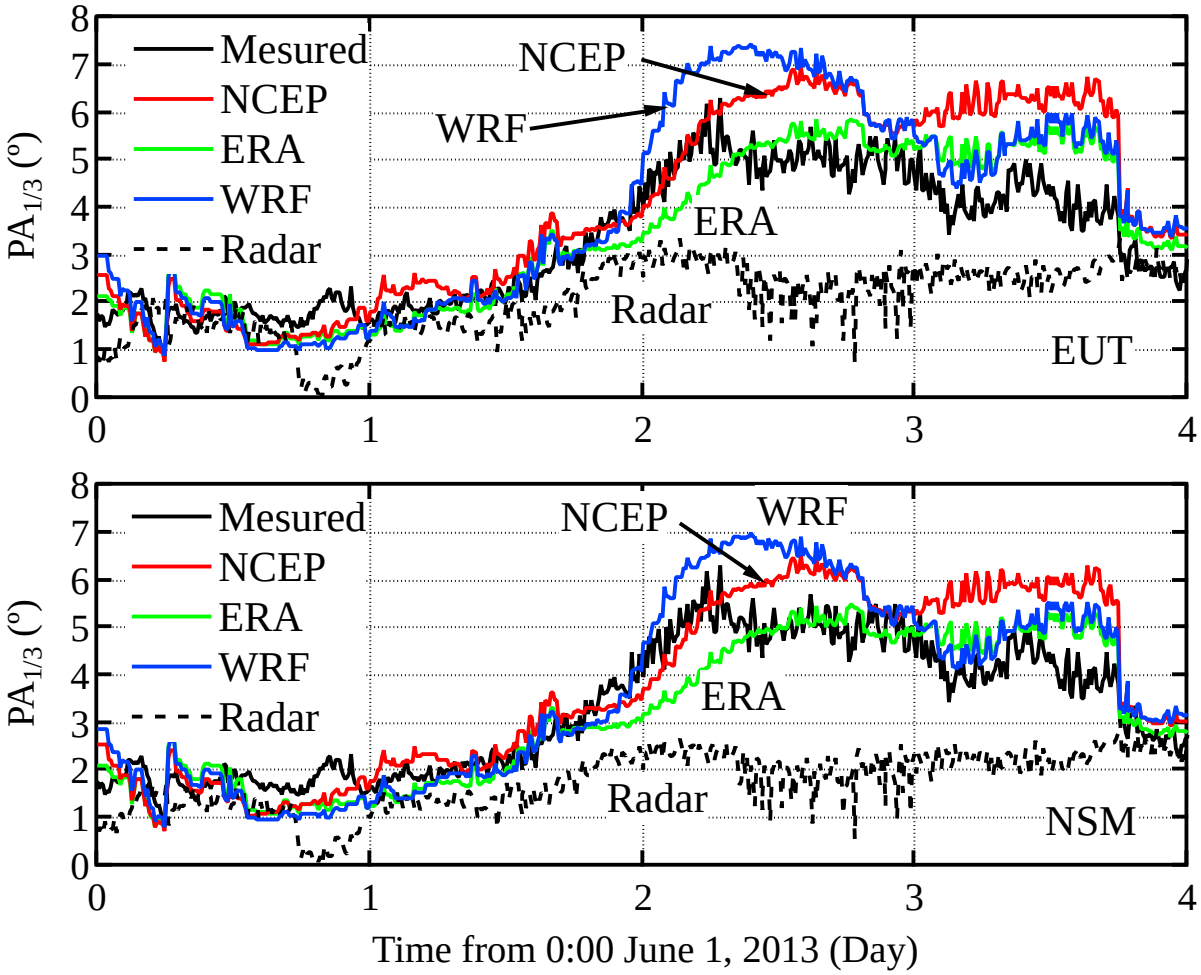

Figure 15 Comparison of observed and calculated pitch motions based on radar measurements and simulated wave hindcasts using EUT (top) and NSM (bottom) methods for Case 1.

Figure 16

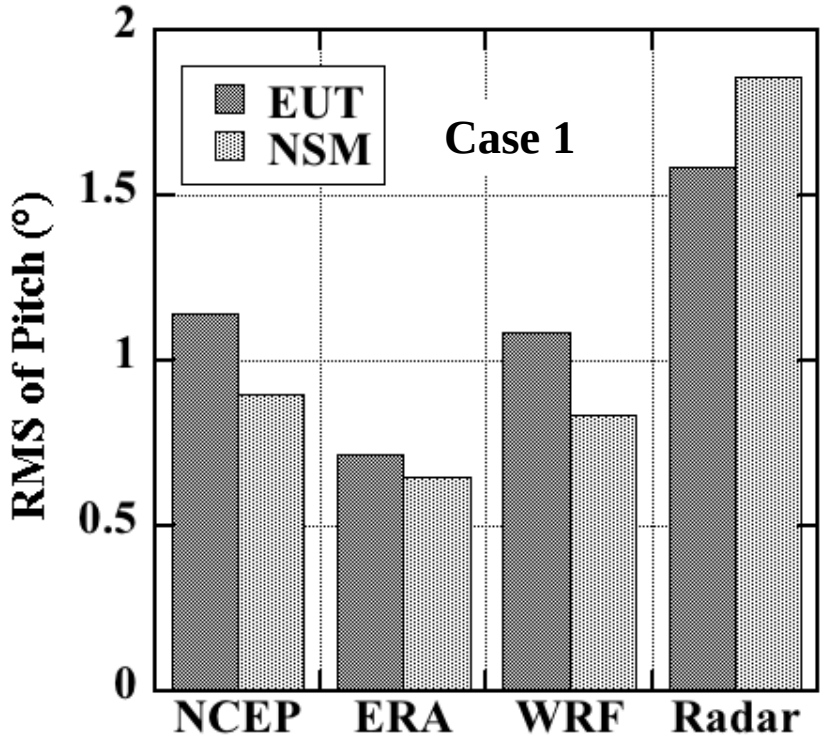

Figure 16 Comparison of RMS of significant pitch amplitude using EUT and NSM methods for Case 1.

Figure 17

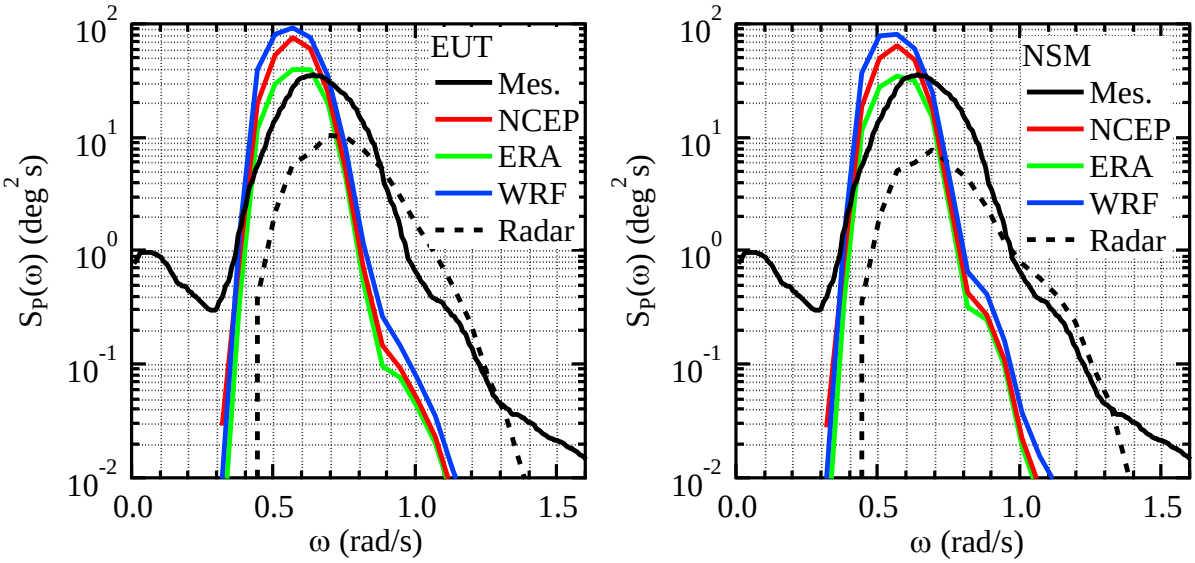

Figure 17 Comparison of observed and calculated pitch frequency spectrums based on radar measurements and simulated wave hindcasts using EUT (left) and NSM (right) methods for case 1 at 6:00 on June 3 2013.

Figure 18

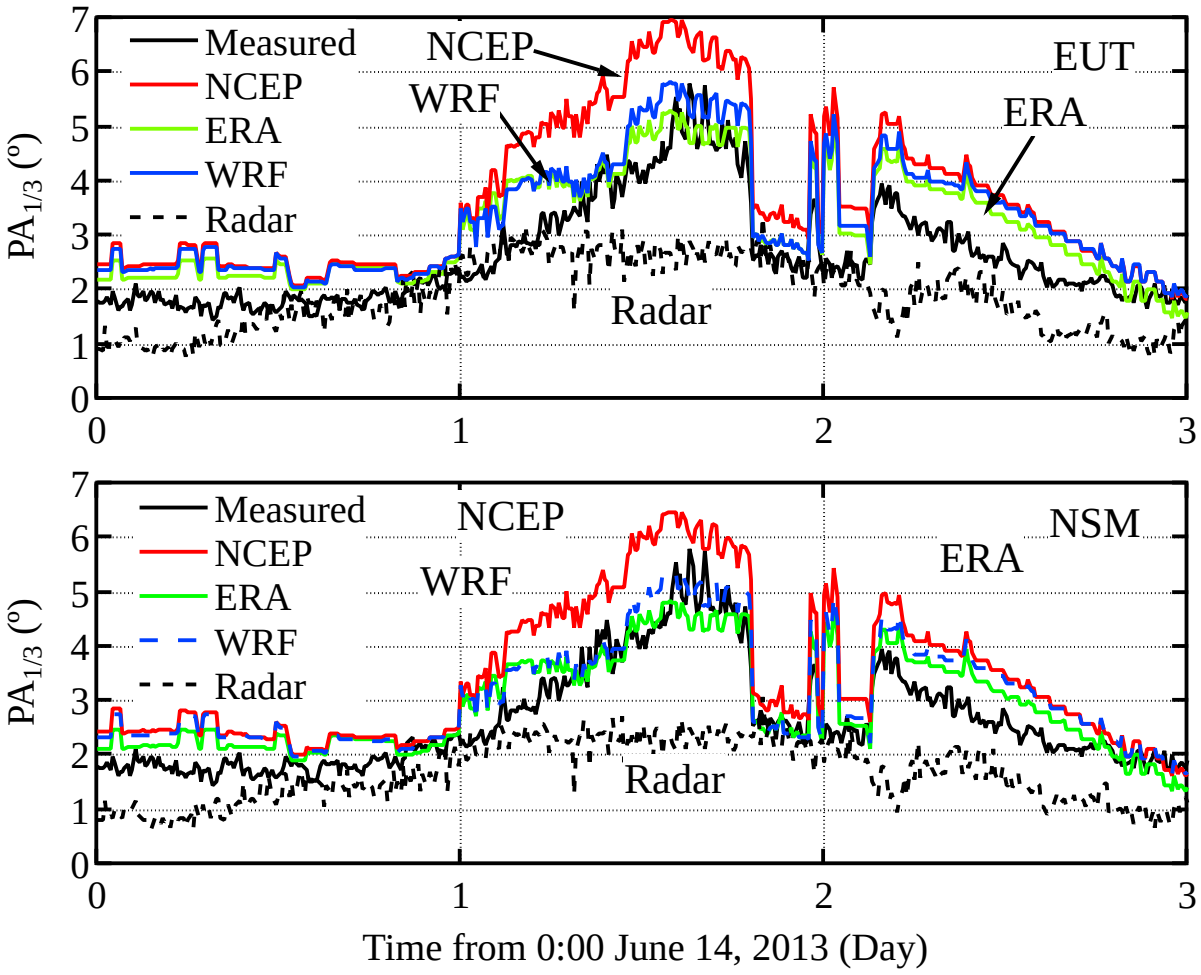

Figure 18 Comparison of observed and calculated pitch motions based on radar measurements and simulated wave hindcasts using EUT (top) and NSM (bottom) methods for Case 2.

Figure 19

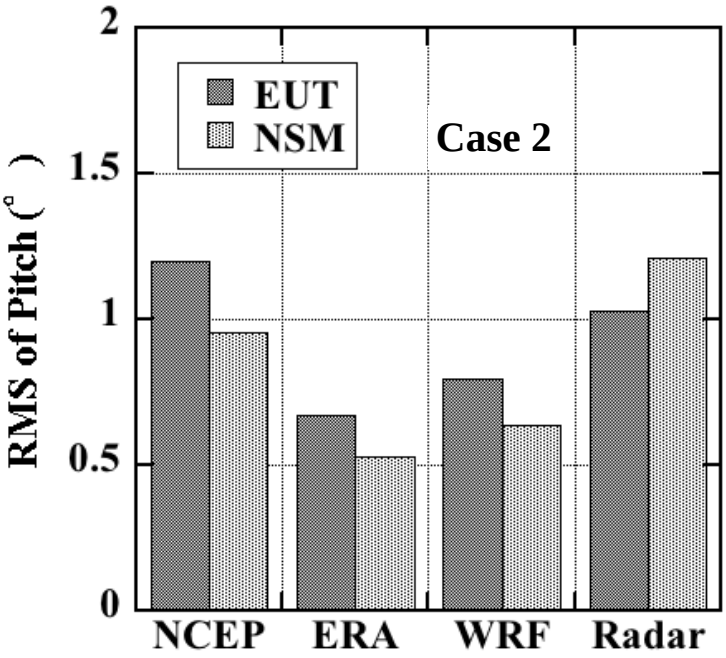

Figure 19 Comparison of RMS of significant pitch amplitude using EUT and NSM methods for Case 2.

Figure 20

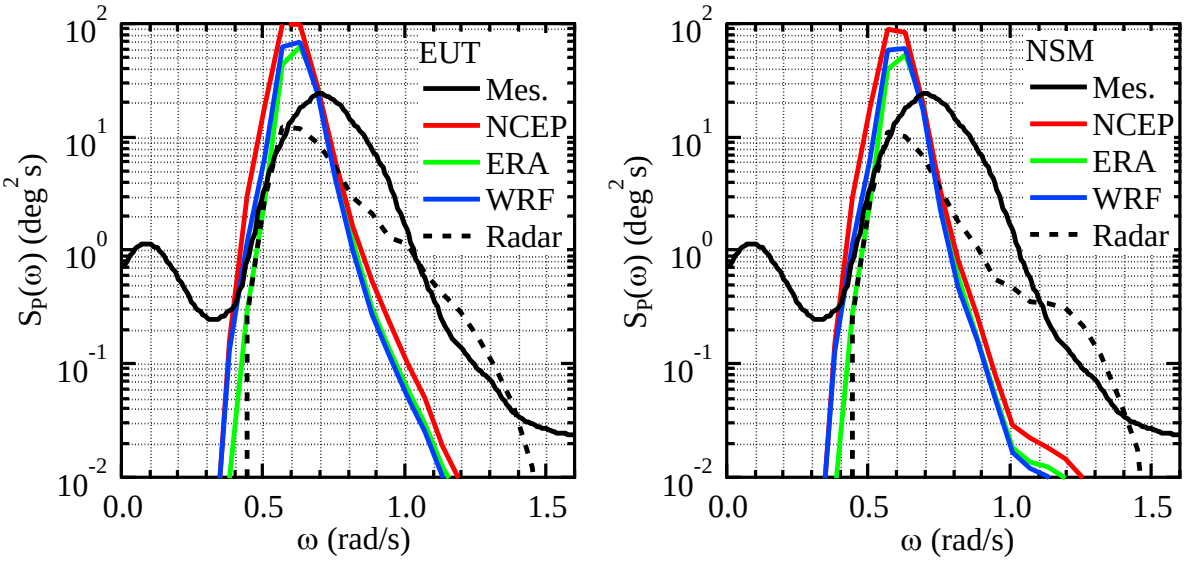

Figure 20 Comparison of observed and calculated pitch frequency spectrums based on radar measurements and simulated wave hindcasts using EUT (left) and NSM (right) methods for Case 2 at 12:00 on June 15 2013.

Figure 21

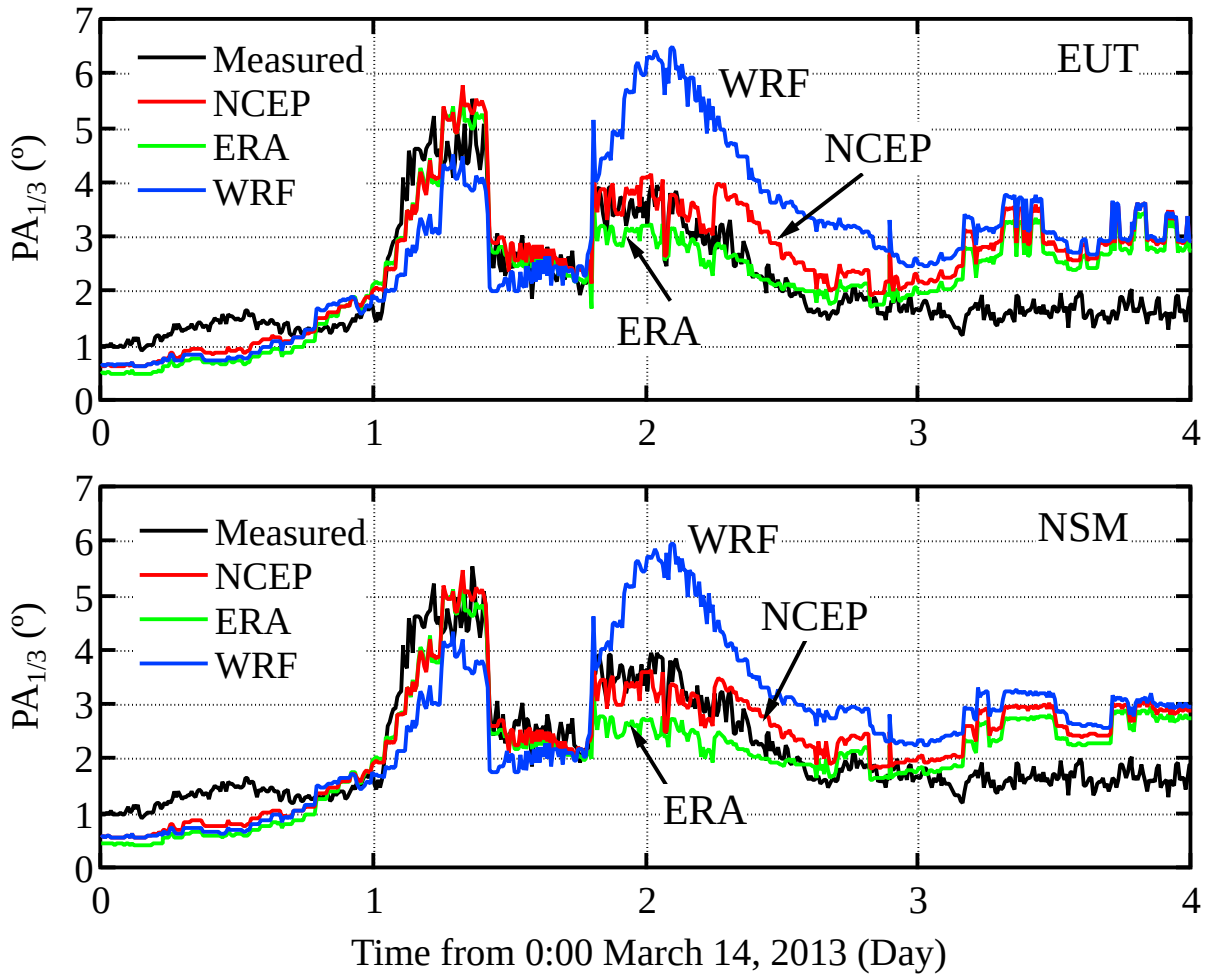

Figure 21 Comparison of observed and calculated pitch motions based on simulated wave hindcasts using EUT (top) and NSM (bottom) methods for Case 3.

Figure 22

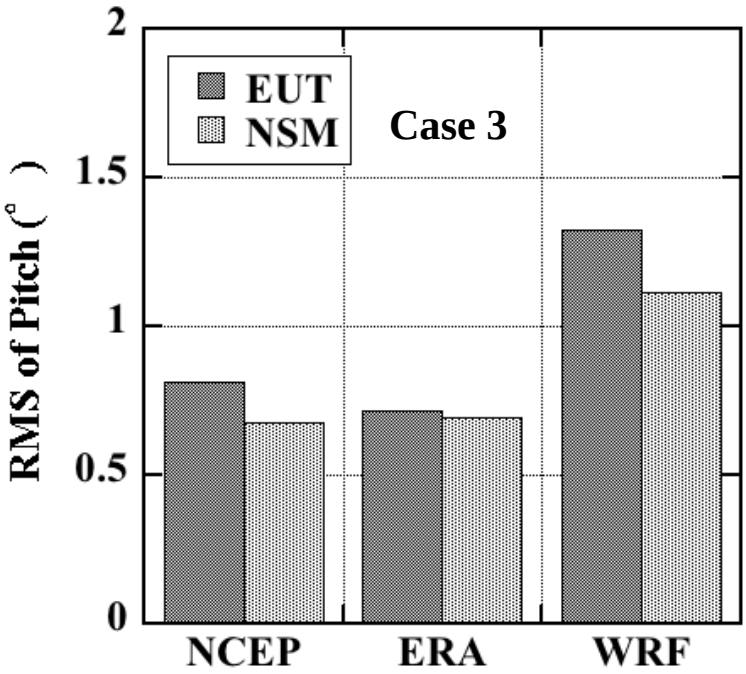

Figure 22 Comparison of RMS of significant pitch amplitude using EUT and NSM methods for Case 3.

Figure 23

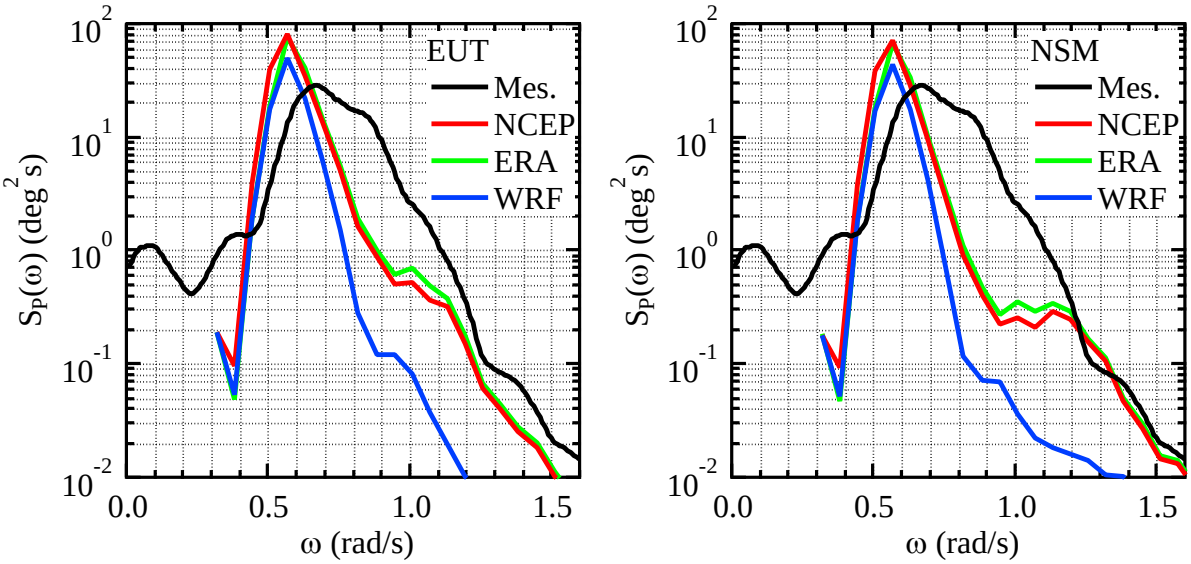

Figure 23 Comparison of observed and calculated pitch frequency spectrums based on simulated wave hindcasts using EUT (left) and NSM (right) methods for Case 3 at 3:00 on March 15 2013.

Table 1

Table 1 Rough-sea navigation periods and corresponding ship conditions for Cases 1, 2, and 3 in 2013

Case	Period	Ship position	Minimum ship speed (knot)	Maximum pitch (°)	Maximum roll (°)
1	Jun 2–4	South coast of South Africa	3.1	5.2	13.8
2	Jun 15	Western South Atlantic Ocean	7.8	5.0	13.7
3	Mar 15–16	Tasman Sea	9.2	4.7	13.7